Rev. Real Academia de Ciencias. Zaragoza. **80:** 47–92, (2025).
ISSN: 0370-3207

Ab-initio thermal transport calculations in single crystals and beyond: a review

Jesús Carrete

https://scholar.google.com/citations?user=6VfkdRwAAAAJ
Instituto de Nanociencia y Materiales de Aragón (INMA),
CSIC-Universidad de Zaragoza, 50009 Zaragoza,
Spain

Premio a la Investigación de la Academia 2025. Sección de Físicas

Abstract

First-principles lattice thermal transport calculations based on the Boltzmann transport equation have emerged, in the last two decades, as a powerful family of methods with high predictive power and wide applicability. This review begins with a summary of the basic ingredients of their formulation and then presents a selection of their applications. The starting point is the relatively simple case of a single crystal in the steady state and then, one by one, the complexities necessary to model realistic devices are introduced, including defects, interfaces and time-dependent processes. Among the examples discussed are nanostructures of all dimensionalities, binary superlattices and high-temperature phases. The main computational bottlenecks of these high-cost calculations, and some of the strategies devised to alleviate them, are also emphasized.

The Boltzmann equation is so exceedingly complex that it seems hopeless to expect to generate a solution from it directly.
[Zim1960]

1 Introduction.

Thermal transport is a fascinating area of study from the point of view of fundamental physics, as well as a critical practical consideration in the design of materials and devices. The concept of heat itself has had a complex historical development and is intricately linked to the second principle of thermodynamics, whose rigorous macroscopic formulation is a recent achievement [LY1999] and whose implications, validity and generalizations in the atomistic world and in connection with quantum information are a matter of intense ongoing research [DS2025]. At the same time, the tendency of areas at different temperatures to achieve balance and the concepts of good and poor thermal conductors are deeply ingrained in our intuition and connected to everyday experience, and have been harnessed by humanity since the very early stages in the development of tool use. Modern technology has only accentuated the importance of understanding and controlling thermal transport. The most paradigmatic domain where this happens is electronics: the notion of thermal throttling — automatic performance reduction to avoid overheating — is well known among consumers of personal computing hardware, thermal management is such a major concern when designing datacenters that the impact of their evaporative cooling systems on local water reserves has become a political question, and simply limiting the temperature swings in power-electronics components of electric vehicles can extend their lifetime [CXH+2023] by more than 60%. While these examples mostly involve the search for improved thermal conductors, tailored thermal insulators are equally necessary, be it to enhance the efficiency of thermoelectric energy recovery [CLM+2014] or as advanced coatings to decrease the working temperature of turbine blades.

The starting point of the modern theoretical study of heat transfer is typically taken as the work of Joseph Fourier [Fou1822], originally published in 1822. In particular, Fourier's law of heat conduction states that the heat current (I_Q) along a block of material suspended between a hot and a cold reservoir is proportional to the difference in temperatures (ΔT) between the reservoirs:

$$I_Q = -G\Delta T. \tag{1}$$

Here, G is the thermal conductance, which is both geometry- and composition- (or structure-

) dependent, and the minus sign accounts for the fact that hot and cold reservoirs act as sources and sinks, respectively. Although other mechanisms of heat transfer, like convection and radiation, also exist, this review will focus on conduction due to its singular importance for crystalline solids. A local form of the law is straightforward to formulate, expressing a generalized linear relationship between the temperature gradient (∇T) and the heat flux ($\boldsymbol{j}_Q$),

$$\boldsymbol{j}_Q = -\boldsymbol{\kappa}\nabla T, \tag{2}$$

where $\boldsymbol{\kappa}$ is the thermal conductivity, which in general is a rank-2 tensor. Fourier's law is analogous to Ohm's law of electric conduction or Fick's law of diffusion in that it expresses a phenomenological linear connection between a thermodynamic force and its corresponding flux. These relations and their connection to entropy production in nonequilibrium thermodynamics were systematically studied by Onsager in the first half of the 20th century [Ons1931]. This more systematic framework also comprises cross phenomena, of which the most important in this context fall under the umbrella of thermoelectricity, i.e., the mutual influences between electric fields ($\boldsymbol{E}$), temperature gradients, heat and electric ($\boldsymbol{j}_e$) currents, expressed by the equations:

$$\begin{aligned}\boldsymbol{j}_e &= \boldsymbol{\sigma}\boldsymbol{E} + \boldsymbol{\sigma}\boldsymbol{S}(-\nabla T)\\ \boldsymbol{j}_Q &= \boldsymbol{\sigma}\boldsymbol{\Pi}\boldsymbol{E} + \left(\boldsymbol{\kappa} + T\boldsymbol{\sigma}\boldsymbol{S}^2\right)(-\nabla T).\end{aligned}$$

The new phenomenological coefficients appearing in these equations are the electric conductivity tensor $\boldsymbol{\sigma}$, the Seebeck coefficient $\boldsymbol{S}$ and the Peltier coefficient $\boldsymbol{\Pi}$, all of them rank-2 tensors. A result of Onsager's theory is that $\boldsymbol{\Pi} = T\boldsymbol{S}$. Although some manifestations of the thermoelectric effects (Seebeck and Peltier) had been known experimentally for more than a century, Onsager's unified treatment opened the door to systematic research into more powerful thermoelectric materials. For example, the maximum performance that can be extracted from a single, homogeneous thermoelectric element operating as an electric generator between a hot and a cold reservoir can be shown to be a monotonically increasing function of its dimensionless thermoelectric figure of merit,

$$ZT = T\frac{\sigma S^2}{\kappa}, \tag{3}$$

where all the coefficients are treated as scalars corresponding to the orientation of the material in the device. This formula motivates the aforementioned search for low-κ materials for thermoelectric applications.

Being able to predict the thermal conductivity tensor of a given material is therefore a primary objective of theoretical and computational materials science as applied to thermal transport. The key ingredient is a microscopic expression of the heat flux that can be calculated and compared with Eq. (2). The first step to achieving such an expression is identifying the mechanisms of energy transfer that may be activated by a temperature gradient. In the specific case of crystalline solids, the main contributors are generally electrons and phonons [Zim1960], although other excitations such as magnons can be relevant in certain materials [LGHC2025]. Many of the applications mentioned in this introduction — in particular, electronic devices and thermoelectric systems — are built from semiconductors, where the charge carrier contribution can be neglected up to very high temperatures, leaving phonons as the dominant heat carriers. Thermal transport by lattice vibrations, and the ab-initio characterization thereof, will be the main object of this review.

I will begin by formulating the phonon contribution to the heat current in a semiclassical setting and continue by obtaining the Boltzmann transport equation for phonons that can provide the non-equilibrium phonon populations necessary to calculate that heat current. Next I will explain how that equation can be solved and how each of the required ingredients can be obtained from ab-initio calculations. This initial explanation will focus on the case of a bulk perfect crystal in the steady state. I will then move on to more complex systems containing defects and nanostructural features, as well as to time-dependent problems. The selection of references and examples is biased towards my own contributions to the field.

2 Basic formulation for pristine crystalline solids.

2.1 The phonon heat current and the linear regime.

Phonons, the low-energy mechanical excitations of a crystal lattice around equilibrium, are bosons that, in rigor, require a fully quantum treatment [SMM2019a]. However, a semiclas-

sical picture, derived heuristically, provides an excellent compromise to tackle problems at a variety of space and time scales. That will be, therefore, be the approach adopted here.

The starting point is a single crystal with a unit cell characterized (at equilibrium) by three linearly independent lattice vectors $(\boldsymbol{\ell}_1, \boldsymbol{\ell}_2, \boldsymbol{\ell}_3)$ and a motif of M atoms placed at positions $\{\boldsymbol{r}_1 \dots \boldsymbol{r}_M\}$. Therefore, the position of an arbitrary atom of the crystal can be expressed as $\boldsymbol{r}_{\boldsymbol{I},i} = \boldsymbol{R}_{\boldsymbol{I}} + \boldsymbol{r}_i$, i.e., as the sum of a lattice vector $\boldsymbol{R}_{\boldsymbol{I}} = I_1\boldsymbol{\ell}_1 + I_2\boldsymbol{\ell}_2 + I_3\boldsymbol{\ell}_3$ for some triplet of integers $\boldsymbol{I} = (I_1, I_2, I_3) \in \mathbb{Z}^3$, and a vector from the motif. If $\boldsymbol{\mathcal{L}}$ is a matrix with the lattice vectors as columns, the columns of $\boldsymbol{\mathcal{R}} = 2\pi\boldsymbol{\mathcal{L}}^{-t}$ are the basis vectors of the reciprocal lattice, formed by all their integer linear combinations.

Each normal mode of the crystal is identified by a vector $\boldsymbol{q}$ in reciprocal space and a branch index $\boxdot \in \{1 \dots 3M\}$, which I will summarize in a compound index $\lambda \coloneqq (\boldsymbol{q}, \boxdot)$. That mode will have an angular frequency ω_λ and a polarization $\boldsymbol{\psi}_\lambda$ (expressed as a finite vector over a finite subset of the crystal). In the second-quantization picture, each phonon carries an energy $\hbar\omega_\lambda$ and a momentum $\hbar\boldsymbol{q}$. The discrete translation symmetry of the crystal in real space endows the functions defined in reciprocal space with periodicity, so each phonon branch $\omega_\boxdot(\boldsymbol{q})$ is completely specified by its values in the first Brillouin zone (BZ), i.e., the Voronoi polyhedron of any point from the reciprocal lattice. Phonons carry energy at a speed corresponding to their group velocity, $\boldsymbol{v}_\lambda = \frac{\mathrm{d}\omega_\lambda}{\mathrm{d}\boldsymbol{q}}$.

A crucial conceptual assumption for this simplified development is that, at each point in space — interpreted in a convenient mesoscopic sense — and for each phonon mode, a time-dependent phonon population $f_\lambda(\boldsymbol{r}, t)$ can be defined, corresponding to a volumetric phonon density f_λ/V for a finite, but large enough, crystal sample of volume V. At thermal equilibrium at a temperature T, that corresponds to the Bose-Einstein distribution with zero chemical potential, $f_{\mathrm{BE},\lambda} = \left(e^{\frac{\hbar\omega}{k_\mathrm{B}T}} - 1\right)^{-1}$. It is convenient to define $f_{1,\lambda} = f_\lambda - f_{\mathrm{BE},\lambda}$, the nonequilibrium component of the population.

In this picture, the energy density around each $\boldsymbol{r}$ due to phonons of mode λ is equal to $\frac{1}{V} f_\lambda \hbar\omega_\lambda$ and the associated heat flux is $\frac{1}{V} f_\lambda \hbar\omega_\lambda \boldsymbol{v}_\lambda$. The total heat flux is obtained by aggregating these contributions:

$$\boldsymbol{j}_Q = \frac{1}{V} \sum_\lambda f_\lambda \hbar\omega_\lambda \boldsymbol{v}_\lambda. \tag{4}$$

Here and in the rest of this review, the notation $\sum_\lambda$ comprises both a literal sum over phonon branches $\boxdot$ and a sum over the $\boldsymbol{q}$ allowed by the boundary conditions of the finite volume, with the latter sum approximated by an integral over the Brillouin zone:

$$\sum_\lambda \coloneqq \frac{V}{(2\pi)^3} \sum_{\boxdot=1}^{3M} \int_{\mathrm{BZ}} \mathrm{d}^3\boldsymbol{q}.$$

The equilibrium component of f_λ obviously cannot create any current, so f_λ can be replaced by $f_{1,\lambda}$ in Eq. (4). To obtain an expression that can be compared with Fourier's law [Eq. (2)], the next step is to assume that the only force driving phonons out of equilibrium is a thermal gradient, and to introduce a linear dependence on ∇T, under the hypothesis that $f_{1,\lambda}$ is a small enough perturbation:

$$f_{1,\lambda} =: -\boldsymbol{F}_\lambda \cdot \nabla T \frac{\partial f_{\mathrm{BE},\lambda}}{\partial T} = -\boldsymbol{F}_\lambda \cdot \nabla T f_{\mathrm{BE},\lambda}(f_{\mathrm{BE},\lambda}+1)\frac{\hbar\omega_\lambda}{k_\mathrm{B}T^2}. \tag{5}$$

Computing the heat current in this simplified setting amounts to obtaining the set of first-order Taylor coefficients $\boldsymbol{F}_\lambda$ for all phonon modes in the system. In fact, inserting Eq. (5) into Eq. (4) yields an explicit expression for the thermal conductivity:

$$\boldsymbol{\kappa}_\ell = \frac{1}{k_\mathrm{B}T^2V} \sum_\lambda f_{\mathrm{BE},\lambda}(f_{\mathrm{BE},\lambda}+1)(\hbar\omega_\lambda)^2 \boldsymbol{v}_\lambda \otimes \boldsymbol{F}_\lambda. \tag{6}$$

I have explicitly added the subscript ℓ to this thermal conductivity to indicate it refers only to the lattice contribution. In metals or in doped semiconductors at high temperature, where the charge carriers also act as significant carriers of heat, the total thermal conductivity can be written as the sum of both contributions: $\boldsymbol{\kappa} = \boldsymbol{\kappa}_\ell + \boldsymbol{\kappa}_\mathrm{ch}$.

2.2 The Peierls-Boltzmann transport equation.

The Boltzmann transport equation (BTE) was formulated by Ludwig Boltzmann [Bol1872] in 1872 to describe the evolution of a distribution of classical pointlike particles over their phase space and over time under the effect of forces, diffusion and binary collisions. The BTE was a landmark in the development of the kinetic theory of gases, and the analysis of

its consequences made an important contribution to the evolution of statistical mechanics, connecting the mechanical/microscopic and thermodynamic/macroscopic worlds. In 1929, Rudolph Peierls adapted the BTE to the study of phonons in solids [Pei1929]. In this section, I will provide a brief derivation of the Peierls-Boltzmann equation, and in the next one I will focus on its specific form used for steady-state calculations in crystalline solids.

The BTE can be considered a specialized form of a master equation for Markovian processes [Rei2016]. The population of state λ is decreased by processes $\lambda \to \lambda'$ that scatter phonons to a different state λ', and increased by processes $\lambda' \to \lambda$ that scatter phonons into λ from a different state. The time evolution of the occupation can thus be expressed, in this abstract formulation, as

$$\frac{\mathrm{d}f_\lambda}{\mathrm{d}t} = \sum_{\lambda' \neq \lambda} w_{\lambda' \to \lambda} f_{\lambda'} - \sum_{\lambda' \neq \lambda} w_{\lambda \to \lambda'} f_\lambda, \tag{7}$$

where $w_{\lambda \to \lambda'}$ is the transition rate from λ to λ' for each phonon. The left-hand side can be expanded as $\frac{\mathrm{d}f_\lambda}{\mathrm{d}t} = \frac{\partial f_\lambda}{\partial t} + \boldsymbol{v} \cdot \nabla_{\boldsymbol{r}} f_\lambda$; note that a possible third term involving a gradient with respect to the momentum does not appear because of the lack of fields exerting a force on phonons, as opposed to e.g. the case of charged particles. For now, the right-hand side can be summarized as $\left(\frac{\partial f_\lambda}{\partial t}\right)_{\text{scatt}}$. With this, the following form of the Peierls-Boltzmann transport is obtained:

$$\frac{\partial f_\lambda}{\partial t} = -\boldsymbol{v}_\lambda \cdot \nabla_{\boldsymbol{r}} f_\lambda + \left(\frac{\partial f_\lambda}{\partial t}\right)_{\text{scatt}}. \tag{8}$$

In the steady state, the time derivative on the left-hand side is zero. Furthermore, under the hypothesis of a small perturbation with respect to equilibrium (necessary for the linear regime to hold), the dominant contribution to $\nabla_{\boldsymbol{r}} f_\lambda$ is $\nabla_{\boldsymbol{r}} f_{\text{BE},\lambda}$. Since the position dependence of the Bose-Einstein term is mediated by the temperature, the phonon BTE in this regime takes a much simpler form:

$$\left(\frac{\partial f_\lambda}{\partial t}\right)_{\text{scatt}} = \frac{\partial f_{\text{BE},\lambda}}{\partial T} \boldsymbol{v}_\lambda \cdot \nabla T. \tag{9}$$

2.3 The linearized phonon BTE for single crystals in the steady state.

Around a potential energy minimum, the potential energy per unit cell of the crystal can be expanded in a Taylor series:

$$E_{\text{pot}} = \frac{1}{2!}\sum_{\substack{\mathbf{0},\boldsymbol{J}\\ i,j\\ \alpha,\beta}} \phi^{(\alpha\beta)}_{\substack{\mathbf{0},\boldsymbol{J}\\ i,j}} u^{(\alpha)}_{\mathbf{0},i} u^{(\beta)}_{\boldsymbol{J},j} + \frac{1}{3!}\sum_{\substack{\mathbf{0},\boldsymbol{J},\boldsymbol{K}\\ i,j,k\\ \alpha,\beta,\gamma}} \phi^{(\alpha\beta)}_{\substack{\mathbf{0},\boldsymbol{J}\\ i,j}} u^{(\alpha)}_{\mathbf{0},i} u^{(\beta)}_{\boldsymbol{J},j} u^{(\gamma)}_{\boldsymbol{K},k} + \dots \tag{10}$$

In this expression, Greek superscripts run over Cartesian axes, and some shorthand notation has been introduced. Specifically, each of the variables denoted as $u^{(\alpha)}_{\boldsymbol{I},i}$ is a component of an atomic position $\boldsymbol{R}_{\boldsymbol{I},i}$, but measured from the equilibrium position $\boldsymbol{R}_{0,\boldsymbol{I},i}$ and scaled by the corresponding atomic mass,

$$u^{(\alpha)}_{\boldsymbol{I},i} \coloneqq \sqrt{m_i}\Big[X^{(\alpha)}_{\boldsymbol{I},i} - X^{(\alpha)}_{0,\boldsymbol{I},i}\Big], \tag{11}$$

and the coefficients of the series are embedded in the so-called order-k interatomic force constants (IFCs),

$$\phi^{(\alpha\beta\dots)}_{\substack{\boldsymbol{I}_1,\boldsymbol{I}_2\dots\boldsymbol{I}_k\\ i_1 i_2\dots i_k\\ \alpha_1,\alpha_2\dots\alpha_k}} \coloneqq \frac{1}{\sqrt{m_{i_1} m_{i_2}\cdots m_{i_k}}}\left(\frac{\partial^k E_{\text{pot}}}{\partial X^{(\alpha_1)}_{\boldsymbol{I}_1,i_1} X^{(\alpha_2)}_{\boldsymbol{I}_2,i_2}\cdots X^{(\alpha_k)}_{\boldsymbol{I}_k,i_k}}\right)_0 = \left(\frac{\partial^k E_{\text{pot}}}{\partial u^{(\alpha_1)}_{\boldsymbol{I}_1,i_1} u^{(\alpha_2)}_{\boldsymbol{I}_2,i_2}\cdots u^{(\alpha_k)}_{\boldsymbol{I}_k,i_k}}\right)_0. \tag{12}$$

The expression in Eq. (10) makes use of the discrete translation symmetry of the lattice to include only IFCs involving unit cell $\mathbf{0}$.

Phonons are the eigenstates of a perfectly harmonic crystal, i.e., one whose Hamiltonian only contains the first term from Eq. (10). Their angular frequencies and polarizations can be obtained from an explicit diagonalization of that Hamiltonian after block-diagonalizing it over a basis adapted to the irreducible representations of the group formed by its translations, leading to the following finite eigenvalue equation at each point in reciprocal space:

$$\boldsymbol{D}(\boldsymbol{q})\boldsymbol{\psi}_\lambda = \omega_\lambda^2 \boldsymbol{\psi}_\lambda, \text{ with } D_{j,k}^{(\alpha\beta)}(\boldsymbol{q}) \coloneqq \sum_{\mathbf{K}} \phi_{\substack{\mathbf{0},\boldsymbol{K} \\ j,k}}^{(\alpha\beta)} e^{-i\boldsymbol{q}\cdot\boldsymbol{R_J}}. \tag{13}$$

$\boldsymbol{D}$, referred to as the dynamical matrix, also contains the group velocity information, as

$$2\omega_\lambda v_\lambda^{(\alpha)} = \boldsymbol{\psi}_\lambda^* \cdot \frac{\partial \boldsymbol{D}(q)}{\partial q^{(\alpha)}} \boldsymbol{\psi}_\lambda. \tag{14}$$

The atomic displacements can also be conveniently reexpressed in terms of creation and annihilation operators of the phonon modes:

$$u_{\boldsymbol{J},j}^{(\alpha)} = \sqrt{\frac{\hbar}{2Mm_j}} \sum_\lambda \left[\boldsymbol{a}_\lambda e^{-i\omega_\lambda t} + \boldsymbol{a}_\lambda^\dagger e^{i\omega_\lambda t} \right] e^{i\boldsymbol{q}\cdot\boldsymbol{R_J}} \frac{\psi_{\lambda,\boldsymbol{J},j}^{(\alpha)}}{\sqrt{\omega_\lambda}}. \tag{15}$$

Any element that breaks either the periodicity or the harmonicity of the Hamiltonian will lead to eigenstates different from pure phonons. However, as long as those elements can be treated as perturbations, the phonon picture will still provide a useful description, but with finite-lifetime phonons due to scattering.

In a typical weakly anharmonic single crystal, phonon scattering is dominated by the third-order term of the Hamiltonian, explicitly presented in Eq. (10). When each of the atomic displacements is expressed as in Eq. (15), that third-order anharmonicity adopts the form of a combination of products of triplets of phonon creation and annihilation operators. Thus, in the second-quantization picture, this term accounts for scattering due to three-phonon processes. Conservation laws restrict the processes that can contribute to only two kinds:

Phonon absorption ($\lambda + \lambda' \to \lambda''$)**:** two phonons are annihilated, one phonon is created.

Phonon emission ($\lambda \to \lambda' + \lambda''$)**:** one phonon is annihilated, two phonons are created.

The conservation laws for energy and momentum take the forms

(16a) $$\omega_\lambda \pm \omega_{\lambda'} = \omega_{\lambda''}, \text{ and}$$

(16b) $$\boldsymbol{q}_\lambda \pm \boldsymbol{q}_{\lambda'} = \boldsymbol{q}_{\lambda''} + \boldsymbol{K_I},$$

where the + and − signs refer to absorption and emission processes, respectively. The conservation of momentum holds in a modular sense, as in the equation above $\boldsymbol{K_I}$ can be any arbitrary vector from the reciprocal lattice. It is possible to make a distinction between *Normal* (N) processes, where $\boldsymbol{K_I} = 0$, and *Umklapp* (U) processes; traditional approximations to the lattice thermal conductivity have often emphasized that distinction as fundamental to their role of anharmonic processes in depressing thermal transport, but many of those conclusions rely on the use of drastic, unphysical simplifications like the Debye model and are in fact myths [MW2014]. The frequency and group velocity, which determine each phonon's contributions to the thermal flux, are well defined regardless of the image of the BZ that is considered, and in modern computational approaches the conservation of momentum is enforced via modular arithmetic with no consideration made to whether a process is N or U; in fact, that classification is not unambiguous, but depends on the choice of unit cell. Direct tests have shown that such approximations based on the N/U dichotomy perform quite poorly [ZA2014].

Inserting Eq. (15) into the third-order term in Eq. (10) and using Fermi's golden rule we obtain a form of the scattering term of the phonon BTE including only third-order anharmonicity:

(17)
$$\begin{aligned}\left(\frac{\partial f_\lambda}{\partial t}\right)_{\text{scatt}} =& \frac{2\pi}{\hbar^2}\sum_{\lambda',\lambda''}^{+}\left|V^{+}_{\lambda\lambda'\lambda''}\right|^2\delta(\omega_\lambda+\omega_{\lambda'}-\omega_{\lambda''})[(f_\lambda+1)(f_{\lambda'}+1)f_{\lambda''}-f_\lambda f_{\lambda'}(f_{\lambda''}+1)]+\\ & \frac{\pi}{\hbar^2}\sum_{\lambda',\lambda''}^{-}\left|V^{-}_{\lambda\lambda'\lambda''}\right|^2\delta(\omega_\lambda-\omega_{\lambda'}-\omega_{\lambda''})[(f_\lambda+1)f_{\lambda'}f_{\lambda''}-f_\lambda(f_{\lambda'}+1)(f_{\lambda''}+1)],\end{aligned}$$

with the matrix elements

(18)
$$V^{\pm}_{\lambda\lambda'\lambda''} = \sum_{\substack{\boldsymbol{J},\boldsymbol{K}\\ i,j,k\\ \alpha,\beta,\gamma}} \phi^{(\alpha\beta\gamma)}_{\mathbf{0},\boldsymbol{J},\boldsymbol{K}\\ i,j,k} \frac{\psi^{(\alpha)}_{\lambda,\mathbf{0},i}\psi^{(\beta)}_{\pm\lambda',\boldsymbol{J},j}\psi^{(\gamma)}_{-\lambda'',\boldsymbol{K},k}}{\sqrt{m_i m_j m_k}}.$$

In both of these expressions, the + and − signs again denote absorption and emission processes, respectively, and the shorthand $-\lambda$ stands for $(-\boldsymbol{q}, \boxdot)$ when $\lambda \coloneqq (\boldsymbol{q}, \boxdot)$. In Eq. (17), + and − over the sums indicate that they only run over processes of the corresponding kind allowed by the conservation of momentum.

The fact that each of the distributions only deviates from its equilibrium value by a small perturbation leads to a more useful, linearized version of the scattering term,

(19)
$$\begin{aligned}\left(\frac{\partial f_\lambda}{\partial t}\right)_{\text{scatt}} =& \frac{2\pi}{\hbar^2}\sum_{\lambda',\lambda''}^{+} \left|V^{+}_{\lambda\lambda'\lambda''}\right|^2 \delta(\omega_\lambda + \omega_{\lambda'} - \omega_{\lambda''}) \times \Big[\\ & (f_{\text{BE},\lambda''} - f_{\text{BE},\lambda}) f_{1,\lambda'} + (f_{\text{BE},\lambda} + f_{\text{BE},\lambda'} + 1) f_{1,\lambda''} + (f_{\text{BE},\lambda''} - f_{\text{BE},\lambda'}) f_{1,\lambda} \Big] + \\ & \frac{\pi}{\hbar^2}\sum_{\lambda',\lambda''}^{-} \left|V^{-}_{\lambda\lambda'\lambda''}\right|^2 \delta(\omega_\lambda - \omega_{\lambda'} - \omega_{\lambda''}) \times \Big[\\ & (f_{\text{BE},\lambda''} - f_{\text{BE},\lambda}) f_{1,\lambda'} + (f_{\text{BE},\lambda'} - f_{\text{BE},\lambda}) f_{1,\lambda''} - (f_{\text{BE},\lambda''} + f_{\text{BE},\lambda'} + 1) f_{1,\lambda} \Big].\end{aligned}$$

This expression is, however, not complete yet, due to a less obvious but crucial perturbation upon the basic harmonic Hamiltonian, namely isotopic disorder. From a physical standpoint, this is interesting for two reasons: firstly, it provides an easily measurable macroscopic manifestation of a nuclear feature whose effect on electrons is, in contrast, very subtle; secondly, it is a source of scattering originating in a breakdown of translation symmetry that, however, does not break the homogeneity of the crystal.

Consider a chemical element with a given isotopic distribution in a given sample (which can be based on natural isotopic abundances, but also controllably altered during manufacturing) characterized by an average mass $\bar{M}$ and a variance σ_M^2. A structure where the occupancy of each site is independent from all others and determined only by the global

isotopic distribution can be modelled as a virtual crystal with a reference Hamiltonian where all atoms of that element are assumed to have mass $\bar{M}$ and each individual atom acts as a point-like perturbation [Tam1983]. From the equation of motion of the system it is straightforward to show that the form of that perturbation is $\frac{\Delta M}{M}\omega^2$, affecting the harmonic term of the Hamiltonian and therefore causing two-phonon (elastic) scattering. Applying Fermi's golden rule again and considering all crystallographic sites with their corresponding elements, Tamura showed in 1983 that the elastic scattering rate between modes λ and λ' due to this mechanism is proportional to $\sum_i \left(\frac{\sigma_{M,i}}{\bar{M}_i}\right)^2 \left|\sum_\alpha \left[\psi^{(\alpha)}_{\lambda,\mathbf{0},i}\right]^* \psi^{(\alpha)}_{\lambda',\mathbf{0},i}\right|^2 \delta(\omega_{\lambda'} - \omega_\lambda)$, and thus essentially determined by the local density of states of the incoming mode at each scattering center [Tam1983]. Adding this contribution to the linearized scattering term of Eq. (19) and using Eq. (5) explicitly delivers the final form of the BTE for a single, weakly anharmonic crystal,

$$\boldsymbol{F}_\lambda = \tau^0_\lambda(\boldsymbol{v}_\lambda + \boldsymbol{\Delta}_\lambda), \tag{20}$$

where the coefficients are defined as

$$\frac{1}{\tau^{(0)}_\lambda} = \sum^{+}_{\lambda'\lambda''} \Gamma^{+}_{\lambda\lambda'\lambda''} + \sum^{-}_{\lambda'\lambda''} \frac{1}{2}\Gamma^{-}_{\lambda\lambda'\lambda''} + \sum_{\lambda'} \Gamma_{\lambda\lambda'} \text{ and} \tag{21a}$$

$$\boldsymbol{\Delta}_\lambda = \sum^{+}_{\lambda'\lambda''} \Gamma^{+}_{\lambda\lambda'\lambda''} \left(\frac{\omega_{\lambda''}}{\omega_\lambda}\boldsymbol{F}_{\lambda''} - \frac{\omega_{\lambda'}}{\omega_\lambda}\boldsymbol{F}_{\lambda'}\right) + \sum^{-}_{\lambda'\lambda''} \frac{1}{2}\Gamma^{-}_{\lambda\lambda'\lambda''} \left(\frac{\omega_{\lambda''}}{\omega_\lambda}\boldsymbol{F}_{\lambda''} + \frac{\omega_{\lambda'}}{\omega_\lambda}\boldsymbol{F}_{\lambda'}\right) + \sum_{\lambda'} \Gamma_{\lambda\lambda'} \frac{\omega_{\lambda'}}{\omega_\lambda}\boldsymbol{F}_{\lambda'}, \tag{21b}$$

and each Γ is a transition rate due to a particular kind of process:

$$\Gamma^{+}_{\lambda\lambda'\lambda''} = \frac{\hbar\pi}{4}\frac{f_{\mathrm{BE},\lambda'} - f_{\mathrm{BE},\lambda''}}{\omega_\lambda\omega_{\lambda'}\omega_{\lambda''}}\left|V^{+}_{\lambda\lambda'\lambda''}\right|^2\delta\left(\omega_\lambda + \omega_{\lambda'} - \omega_{\lambda''}\right) \tag{22a}$$

$$\Gamma^{-}_{\lambda\lambda'\lambda''} = \frac{\hbar\pi}{4}\frac{f_{\mathrm{BE},\lambda'} + f_{\mathrm{BE},\lambda''} + 1}{\omega_\lambda\omega_{\lambda'}\omega_{\lambda''}}\left|V^{-}_{\lambda\lambda'\lambda''}\right|^2\delta\left(\omega_\lambda - \omega_{\lambda'} - \omega_{\lambda''}\right) \tag{22b}$$

$$\Gamma_{\lambda\lambda'} = \frac{\pi\omega_\lambda^2}{2}\sum_i\left(\frac{\sigma_{M,i}}{\bar{M}_i}\right)^2\left|\sum_\alpha\left[\psi^{(\alpha)}_{\lambda,\mathbf{0},i}\right]^*\psi^{(\alpha)}_{\lambda',\mathbf{0},i}\right|^2\delta(\omega_{\lambda'} - \omega_\lambda). \tag{22c}$$

This is now a large set of algebraic linear equations for the $\boldsymbol{F}_\lambda$ with completely explicit expressions for all the coefficients, which in principle can be solved. The details of the solution method will be discussed in the next section; however, it is worth mentioning that historically this was still considered a nearly impossible task. Clear evidence of this, in addition to the quote from Ziman that opens this article, is that Callaway [Cal1959] wrote in 1959 that "Although an exact calculation of lattice thermal conductivity is possible in principle, lack of knowledge of crystal vibration spectra and of anharmonic forces in crystals and the difficulty of obtaining exact solutions of the Boltzmann equation are formidable barriers to progress." One of the most usual workarounds was working under the so-called relaxation time approximation (RTA), where each phonon mode λ is assumed to relax to thermal equilibrium through a single kind of process, whose characteristic time is therefore equal to that mode's lifetime. The inverse of that lifetime is the total scattering rate of the mode, that is, the sum of the scattering rates of all independent scattering processes, which is precisely what Eq. (21a) expresses. Indeed, the RTA amounts to assuming that $\boldsymbol{\Delta}_\lambda = 0$ in Eq. (20), yielding the explicit solution $\boldsymbol{F}_\lambda = \tau^{(0)}_\lambda\boldsymbol{v}_\lambda$. This can be substituted into Eq. (6) to recover the well know (but merely approximate) expression for the thermal conductivity in the RTA:

$$\boldsymbol{\kappa}_\ell = \frac{1}{k_\mathrm{B}T^2V}\sum_\lambda f_{\mathrm{BE},\lambda}(f_{\mathrm{BE},\lambda} + 1)(\hbar\omega_\lambda)^2\boldsymbol{v}_\lambda\otimes\boldsymbol{v}_\lambda\tau^{(0)}_\lambda. \tag{23}$$

For many common semiconductors, the RTA incurs an error in the conductivity of 10% or less [WBSD2009], even if the individual non-equilibrium populations may be quite inaccurate. However, for high-conductivity systems like diamond the results can be much more dramatically wrong [WB2010].

While the RTA eliminates the problem of solving the linearized BTE, it does not alleviate the burden of obtaining all the ingredients needed to compute the coefficients. Thus, the historical trend before first-principles approaches became available was to use parameterized forms of $\tau_\lambda^{(0)}$, often based on analytical assumptions like the Debye model and valid only for small $|\boldsymbol{q}|$. Such methods require fitting their parameters to experimental data and therefore lack predictive power, but even with the best fitting their performance is often poor due to their limited flexibility.

2.4 Solving the linearized BTE.

The first practical method to solve the system of linear equations and obtain the non-equilibrium populations was proposed in 1996 by Omini and Sparavigna [OS1996]. It is a simple iterative strategy that starts from the RTA result $\boldsymbol{F}_\lambda^{(0)} = \tau_\lambda^{(0)} \boldsymbol{v}_\lambda$ and then enters a loop where $\boldsymbol{\Delta}_\lambda$ is evaluated according to Eq. (21b) and then its value is substituted into Eq. (20) to obtain a new estimate of $\boldsymbol{F}_\lambda$ for the next iteration, until convergence is achieved. In the decade that followed, the Omini-Sparavigna method was applied to some systems using mostly application-specific code and interaction models of varying quality (e.g. [BMB+2007; WB2010; WBSD2009]). However, the first public general-purpose software package for this purpose was `ShengBTE` [LCKM2014], released in 2014 and of which I am a coauthor. I will describe the steps of the solution algorithm as implemented in `ShengBTE`:

1. A Γ-centered discrete regular grid of $N_1 \times N_2 \times N_3$ $\boldsymbol{q}$ points is built to sample the Brillouin zone.

2. The space group of the system is detected using the `spglib` library [AT2024] and its elements used to split the $\boldsymbol{q}$ points into equivalence classes.

3. At each point in the grid the angular frequencies, group velocities and polarizations of all phonon branches are obtaining. They are then explicitly symmetrized over equivalence classes.

4. Using Tamura's formula, the contribution to phonon scattering from isotopic disorder is calculated.

5. A search for allowed three-phonon processes is run by iterating over all possible pairs of $\boldsymbol{q}$ and $\boldsymbol{q}'$, using the conservation of momentum to compute the $\boldsymbol{q}''$ that might complete valid absorption or emission processes, and then checking all triplets formed by a phonon mode at each point to see if they can satisfy the conservation of energy. The condition in Eq. (16a) will never be fulfilled exactly by three modes sampled from the grid, and each $\boldsymbol{q}$ point actually stands for the area of the BZ around it, so a tolerance must be applied in this search. `ShengBTE` uses a parameter-free, locally adaptive regularization [LML+2012] of the Dirac δ in Eqs. (22b) and (22a) to accomplish this without losing predictive power.

6. The scattering amplitude for each of the allowed processes is calculated according to Eqs. (22a) and (22b).

7. The Omini-Sparavigna iterative scheme is set up and run until convergence.

8. The thermal conductivity is computed and symmetrized as a rank-2 tensor.

This outline is somewhat simplified and omits many additional harmonic and anharmonic results calculated during a typical run [LCKM2014].

The publication introducing ShengBTE has been cited almost 3000 times, the program having been used with success for many different kinds of crystals, both experimentally known and hypothetical. A typical example for a relatively simple semiconductor, InAs, is shown in figure 1. Crucial to this success is the thorough and automatic integration of the symmetries in reciprocal space, since small deviations from the perfect symmetry can derail the convergence or yield completely unphysical results.

Most of the computational cost of the algorithm, in terms of both CPU and memory, comes from the detection of allowed processes and the calculation of their amplitudes, since the numbers of absorption and emission processes typically range from 10^7 to 10^{10}. Fortunately, it can be parallelized over $\boldsymbol{q}$ and over phonon processes.

More recent phonon BTE solvers, like almaBTE [CVK+2017] have tended to move on from the Omini-Sparavigna iterative algorithm and use either a direct solver of the linear system or a more standard, general-purpose iterative approach. Those procedures generally result in a more stable and accurate solution.

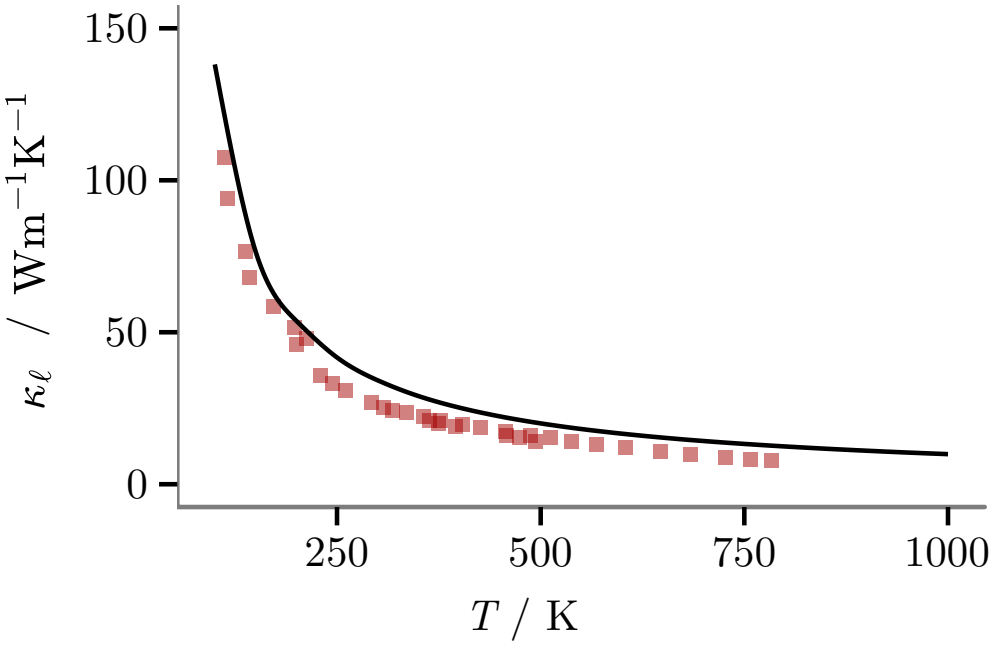

Figure 1: Thermal conductivity of bulk InAs computed using `ShengBTE` (solid line) compared to data from multiple experiments (red squares) [BUBC1959; LA1972; OPG1972; TS1971]. Plot reconstructed with data from [LCKM2014].

2.5 Obtaining the IFCs and other ingredients of the BTE.

Based on the expressions handled in the preceding section, and besides some tabulated quantities like atomic masses and isotopic distributions, the inputs needed to fully formulate the BTE are the equilibrium atomic positions and a set of second- and third-order derivatives of the potential energy at those positions, i.e., the harmonic and anharmonic IFCs. To keep the method parameter free, it is desirable to extract those pieces of information from ab-initio calculations, and due to its favorable tradeoffs between accuracy and scalability, methods based on density functional theory (DFT) have become the standard choice.

DFT [PY1989] is a reformulation of the electronic problem in terms of a single scalar field, the electronic density, which therefore avoids the exponential scaling barrier of wavefunction-based methods [Koh1999]. Although DFT is formally an exact theory for the ground state, in practice the need to use relatively simple approximations to the so-called exchange and correlation terms of the Hamiltonian places some important practical limitations on its precision and accuracy [Fei2010]. Some of those limitations are systematic,

such as a tendency to underestimate electron localization (mispredicting semiconductors as metals) and its neglect of van-der-Waals-like interactions, and there are approximate strategies to correct for those; however, others are system-dependent and sometimes difficult to detect.

The many DFT implementations available differ in what kind of functions they use to represent the solution (the basis), the techniques they offer to abstract away the core electrons (pseudopotentials, plane-augmented waves or PAW…), the platform they are implemented on, the amount of postprocessing they are able to do, whether they are proprietary or open-source, and so on and so forth. Software based on the PAW formalism [Blö1994], using plane waves for its basis, is particularly well suited for the efficient and accurate study of bulk crystals, and is therefore the most popular choice for phonon calculations. The main representatives of this category are `VASP` [KF1996] on the proprietary side, and `Quantum ESPRESSO` [GBB+2009] among open-source packages.

A typical DFT calculation takes atomic positions as input and outputs the total energy and the forces on each atom — the latter being relatively inexpensive to obtain through the Hellmann-Feynman theorem — as well as the stress tensor on the simulation box. That information can be used to run a local, possibly constrained, minimization to reach an equilibrium configuration. From that starting point, in very broad terms there are three families of approaches to obtain the IFCs:

Density-functional perturbation theory (DFPT): A perturbation, be it a displacement of a single atoms or a periodic displacement with a periodicity corresponding to $\boldsymbol{q}$, can be applied to the DFT Hamiltonian and the corresponding changes to the energies and wave functions of the eigenstates studied with the methods of perturbation theory [BdGDG2001]. Doing so up to the first order, the Hellmann-Feynman theorem can be recovered, the second order makes possible to extract the dynamical matrix $\boldsymbol{D}(\boldsymbol{q})$, and the third order opens the door to obtaining anharmonic information as well. A crucial result is the $2n + 1$ theorem, which states that the n-th derivative of the wave functions is needed to access up to the $(2n + 1)$-th perturbation to the energy, making the calculation of $\boldsymbol{D}(q)$ significantly more costly than that of the forces.

Finite differences: A second-order IFC can be approximated by a suitable difference between two forces on atoms in different configurations. For instance, the xy force

constant between two atoms i and $j \neq i$ can be estimated as

$$K_{i,j}^{(xy)} = \frac{1}{\sqrt{m_i m_j}} \frac{\partial^2 E_{\text{pot}}}{\partial x_i \, \partial y_j} \simeq \frac{1}{\sqrt{m_i m_j}} \frac{f_i^{(x)}(y_j = y_{j,0} - h) - f_i^{(x)}(y_j = y_{j,0} + h)}{h},$$

where h is an appropriately small displacement (typically in the order of 10^{-2} Å), $f_i^{(x)}$ is the x component of the force on atom i, and all coordinates other than y_j are assumed to retain their equilibrium values. Two DFT runs, with atom j in different positions, are needed, although one is enough if a (less accurate) single-sided finite-difference formula is deemed acceptable. Similar expressions can be developed for IFCs of any order, and specifically the third.

Regression: The Taylor expansion in Eq. (10), when truncated to any given order, can be regarded as a linear equation with the IFCs as unknowns and products of the $u_{\boldsymbol{J},j}^{(\beta)}$ as coefficients. The same applies to the derivative of that equation with respect to one of the displacements. Therefore, if DFT results are available for the right number of different configurations of atomic displacements, a system of linear equations with forces as its independent term and products of displacements as coefficients can be formulated and solved to obtain the IFCs. That would constitute a small variation on the finite-difference approach described above, but this idea comes onto its own when it is formulated as a fit instead of just a system of equations. By formulating a loss function that quantifies the differences between the DFT forces and those obtained from the finite Taylor expansion and minimizing that loss subject to constraints, the best-fit IFCs can be obtained with a controlled tradeoff between quality and computational effort. In particular, a sparsity constraint can be applied to employ fewer (and possibly far fewer) calculations than would be demanded by the finite-difference formulas, while still recovering satisfactory values of the most important IFCs up to the desired order [ZNXO2014].

DFPT-based methods are theoretically appealing but incur significant implementation costs, specifically due to the need to evaluate derivatives of the different mathematical components of the DFT-based methods being used in each calculation. The magnitude of those costs comes into relief when the large variety of exchange and correlation functionals, kinds of pseudopotentials, types of spin configurations (unpolarized, collinear or non-collinear),

iterative methods and so on that a single DFT package may implement is taken into account. Adding a new feature to the program becomes much more complex if everything must be kept DFPT-compatible. It is thus understandable that full second-order DFPT implementations for phonon calculations are relatively scarce, and third-order implementations are even more exceptional. The best example is `D3Q` [PML2013], part of the `Quantum ESPRESSO` ecosystem. The program imposes strong restrictions on the underlying DFT calculations: no spin polarization, no noncollinear magnetism, no ultrasoft pseudopotentials or PAW are allowed [GAB+2017]. Moreover the performance of the method is not good enough to directly extract $\boldsymbol{D}(\boldsymbol{q})$ at every point of the relatively dense grid employed in the solution of the BTE: a sparser sampling is used instead, which is then transformed back to real space, resulting in a set of second-order IFCs from which $\boldsymbol{D}(\boldsymbol{q})$ can be interpolated at any other $\boldsymbol{q}$ point.

In contrast, the finite-difference and regression-based methods can be implemented on top of any DFT package capable of calculating forces on atoms in arbitrary configurations, and therefore enables access to most of the power of those implementations, including beyond-DFT corrections. Likewise, a package can be designed that is able to interface with several or many DFT backends, and it is easy to extend it to new backends. A very user-friendly and fully featured example of such a package is `Phonopy` [TT2015], widely used in finite-difference calculations of second-order IFCs. For third-order calculations, one of the possibilities is `thirdorder.py` [LCKM2014], designed to be used with `ShengBTE`. Regarding regression methods, `hiPhive` [EFE2019] is an open-source implementation of a wide array of feature selection and compressive-sensing methods enabling access to IFCs of arbitrary order at reasonable cost.

DFT calculations for bulk crystals are performed using a finite simulation box — often either an irreducible or a conventional unit cell — and periodic boundary conditions. Strictly speaking, this is incompatible with representing a configuration where a single atom is displaced with respect to equilibrium (like those entering the finite-difference formulas), since all of the periodic images of that atom will be displaced in the same fashion. To obtain even a reasonable approximation, a supercell containing multiple instances of that unit cell needs to be constructed. The simplest and most usual case involves a diagonal supercell, in which the unit cell is repeated $s_1 \times s_2 \times s_3$ times along the crystallographic axes. The forces computed in such a supercell still contain artifacts of periodicity, but it is

straightforward to show [PLK1997] that the dynamical matrix computed from those cumulant force constants matches the exact one at the $s_1 \times s_2 \times s_3$ $\boldsymbol{q}$ points of the Brillouin zone that are commensurate with the supercell. At any other point, $\boldsymbol{D}(\boldsymbol{q})$ can be considered an interpolation. The quality and the cost of the approximation both increase with supercell size.

A crucial part of the practical deployment of any of these methods is the use of crystal symmetry, both to reduce the number of DFT runs and to ensure the physical correctness of the result. From the point of view of a supercell, any operation from the crystal's space group amounts to the combination of a (possibly improper) rotation and an atomic permutation. The n-th order IFCs must transform as a rank-n tensor under the effect of these operations, but the transformed values must be identical to the untransformed ones. Thus, each symmetry operation defines a set of homogeneous linear constraints that the IFCs must fulfill [LCKM2014; PLK1997]. In other words, the IFCs are restricted to belong to the nullspace of the homogeneous system of linear equations induced by the space group. Therefore, to determine the full IFC tensor it is enough to determine a set of coefficients to build the right linear combination of the elements of a basis of that nullspace. This, combined with the fact that each DFT run outputs $3M$ different force components, and the invariance of mixed partial derivatives under an exchange of the order of differentiation, enables drastic reductions in the number of DFT runs required by a calculation: the full phonon spectrum of Si can be extracted from DFT forces for a single configuration, and a sufficient set of third-order IFCs for the 6H phase of SiC (comprising 56754 elements) require just 216 runs.

The continuous symmetries of free space cannot be ignored in IFCs calculations either: rigid rotations and translations of the full crystal cannot change the energy of the system or generate any forces. Inserting the condition of zero forces under translations into Eq. (10) yields an additional set of homogeneous linear equations known as the acoustic sum rules (ASRs). Unfortunately, IFCs obtained from DFT contain artifacts that cause large departures from the ASRs and require corrections. Failure to fix those deviations will cause the phonon spectrum to lack true acoustic branches that have zero angular frequencies at the Γ point, a feature so critical from a physical standpoint that phonon spectra containing such artifacts can be considered useless. Similarly, third-order IFCs that violate the ASRs give rise to unphysical anharmonic scattering rates with the wrong behavior in the $\omega \to 0$

limit. Symmetrization of the IFCs to satisfy the ASRs can be performed a posteriori, using a least-squares criterion to keep the changes to a minimum; alternatively, the ASRs can be directly added to the linear system derived from the discrete symmetries.

A more fundamental limitation of the supercell approach is its inability to capture long-range interactions, and specifically electrostatic interactions. The consequences are significant for compounds with polar bonds: figure 2 (left) illustrates this for the example of rocksalt PbS, with a sequence of calculations with supercells of increasing size. I have chosen particularly elongated supercells along a single axis to obtain large numbers of commensurate $\boldsymbol{q}$ points along the corresponding direction in reciprocal space. From this sequence it is obvious that, even with those extreme sizes, the calculation is not well converged with respect to supercell size, and shows no sign of convergence. In particular, the longitudinal and transverse optical branches (LO and TO, depicted in red and brick colors) always have the same frequency at Γ but are no longer degenerate at the first commensurate point away from Γ, no matter how close that point gets. To solve this properly, a nonanalytic correction (NAC) needs to be added to the dynamical matrix to account for those interactions that cannot be captured by any supercell. The result is shown in the right-hand-side panel of figure 2, confirming that the LO/TO split begins at Γ and is much wider than could be expected from the supercell calculations.

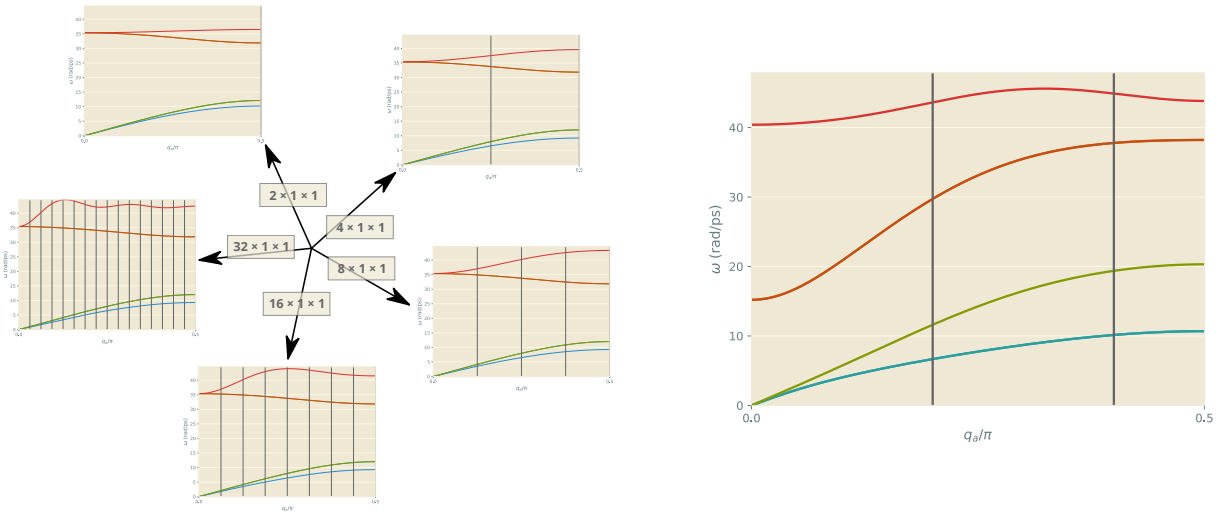

Figure 2: Left: Evolution of the phonon spectrum of rocksalt PbS along the $\Gamma \to X$ direction estimated using supercell-calculated IFCs with different supercell sizes. The vertical bars represent commensurate $\boldsymbol{q}$ points. Right: Same spectrum, computed using a $5 \times 5 \times 5$ supercell and a nonanalytic correction.

There are several different approaches to the NAC [GAT1994; GL1997; WWK+2010], but they generally share a common set of ingredients: the high-frequency dielectric tensor of the crystal ($\boldsymbol{\varepsilon}$) and the Born effective charge tensors [Spa2012] for all atoms, defined as $Z_i^{(\alpha\beta)} = \frac{1}{e}\frac{\partial p^{(\beta)}}{\partial X_i^{\alpha}}$, where $\boldsymbol{p}$ is the electric dipole moment of the solid. Mainstream plane-wave DFT codes can provide access to those quantities through DFPT [GHK+2006]. An important feature of the NAC, which gives it its name, is that the correction depends on matrix elements such as $\boldsymbol{q}\cdot\boldsymbol{\varepsilon}\boldsymbol{q}$ and $(\boldsymbol{Z}_i\boldsymbol{q})\cdot(\boldsymbol{Z}_j\boldsymbol{q})$ that need not have a well defined $\boldsymbol{q}\to\boldsymbol{0}$ limit; thus, the optical frequencies near Γ are direction-dependent, and finite jumps can appear in a band diagram along a path that crosses that point.

In summary, the most well-established recipe to obtain all the ingredients of the BTE from ab-initio calculations involves using a plane-wave-based DFT engine to run three series of calculations, not counting the minimization: a short series of runs to compute the second-order IFCs, a perturbative calculation to extract the dielectric parameters, and a much longer series to obtain the third-order IFCs, but regression-based approaches can merge the first and last of these with significantly lower cost.

3 Extensions.

3.1 Defect-laden crystals.

Although pristine semiconductor samples — and even isotopically pure ones — are experimentally accessible and serve as a benchmark of ab-initio-based phonon BTE calculations, they are not the most frequently found kind of sample in practical use. As a matter of fact, control of defects is an integral part of semiconductor technology, whether they be an accidental result of the synthesis procedure or introduced on purpose. As an example of the former, part of the contributions leading to Shuji Nakamura's 2014 Nobel Prize for co-inventing the blue LED was related to the reduction of dislocation density [Nak2015]. As for the intentional introduction of defects, it is the mechanism behind doping, key to modulating the electrical and optical properties of semiconductors. In thermoelectricity, an application where the thermal conductivity is a primary design consideration, doping densities are extremely high (often in the order of $10^{21}\,\mathrm{cm}^{-3}$). It is therefore desirable to extend the success of phonon BTE calculations to defect-laden samples while retaining their high predictive power.

Defects come in many shapes and types, which can be classified according to their

dimensionality. 0D defects are confined in a region of a size comparable to a few interatomic distances along all directions, and include vacancies, substitutions, interstitials, antisites, and so on. 1D defects are extended along a particular direction, the best known example being dislocations. Finally, 2D defects, extended along two different directions, comprise boundaries and interfaces.

A common feature of defects is that they break the periodicity of the crystal structure, and therefore they act as a perturbation to the harmonic part of the Hamiltonian, introducing elastic scattering. This was also the case with isotopic disorder (which is, in fact, a particular distribution of defects); however, as opposed to that case and to many instances in the theory of electron scattering, the magnitude of the perturbation is such that Fermi's golden rule is not applicable [KCLM2014], and fully converged perturbation theory must be used. The central object in this treatment is the t matrix,

$$\boldsymbol{t} = \left(\mathbf{1} - \boldsymbol{V}\boldsymbol{g}^{+}\right)^{-1}\boldsymbol{V}, \tag{24}$$

which encodes both the information about the perfect system where the defect is embedded (through its causal Green's function, $\boldsymbol{g}^{+}$) and the perturbation itself (in the perturbation matrix, $\boldsymbol{V}$). The elastic scattering rates, $\Gamma_{\lambda\lambda'}$, can be extracted from $\boldsymbol{\psi}^{*}_{\lambda'} \cdot \boldsymbol{t}\boldsymbol{\psi}_{\lambda}$, instead of from $\boldsymbol{\psi}^{*}_{\lambda'} \cdot \boldsymbol{V}\boldsymbol{\psi}_{\lambda}$ as in Eq. (22c). However, it is more efficient, generally sufficient, and therefore customary to include phonon-defect scattering only at the RTA level and use the optical theorem [Eco2006] to compute their contribution to the scattering rate,

$$\tau^{-1}_{\lambda,\mathrm{def}} = -\frac{n_{\mathrm{def}} V_{\mathrm{uc}}}{\omega_{\lambda}} \operatorname{Im}\{\boldsymbol{\psi}^{*}_{\lambda} \cdot \boldsymbol{t}\boldsymbol{\psi}_{\lambda}\}, \tag{25}$$

where V_{uc} is the unit cell volume and n_{def} is the volumetric concentration of defects.

For spatially confined defects, Eq. (25) can be evaluated in real space. The 3×3 block of the Green's function connecting atoms $(\boldsymbol{I}, i)$ and $(\boldsymbol{J}, j)$ is defined as

$$\underset{i,j}{\boldsymbol{g}^{+}_{\boldsymbol{I},\boldsymbol{J}}}(\omega) = \lim_{\epsilon \to 0^{+}} \sum_{\lambda} \frac{\boldsymbol{\psi}_{\lambda,\boldsymbol{I},i}\boldsymbol{\psi}^{\dagger}_{\lambda,\boldsymbol{J},j}}{\omega^2 + i\epsilon - \omega^2_{\lambda}}, \tag{26}$$

and the singular form of the denominator demands very specific integration techniques. For bulk crystals, the usual choice is the linear tetrahedron method (introduced in [LV1984], but see [Eye2012] for formulas correcting some typos in the original). It starts by subdividing each minizone defined by a $s_1 \times s_2 \times s_3$ sampling of the BZ into six nonoverlapping tetrahedra. Then, the frequencies of each phonon band are linearly interpolated within each tetrahedron, starting from their values at the four corners and using barycentric coordinates. Those integrals and their $\epsilon \to 0^+$ can be solved analytically, and the total $\boldsymbol{g}^+$ is recovered a sum of the contributions from each tetrahedron. The other ingredient of the calculation is the perturbation matrix, which contains two contributions: the first, $V_{\boldsymbol{M}}$ from the mass difference of the defect with respect to the host system, with the same form as in the case of isotopic disorder, and the second, $V_{\boldsymbol{K}}$, from the difference in second order IFCS:

$$V^{(\alpha\beta)}_{\boldsymbol{K},\substack{\boldsymbol{I},\boldsymbol{J}\\i,j}} \coloneqq K^{(\alpha\beta)}_{0,\substack{\boldsymbol{I},\boldsymbol{J}\\i,j}} - K^{(\alpha\beta)}_{\substack{\boldsymbol{I},\boldsymbol{J}\\i,j}}. \tag{27}$$

The IFCs of the perfect and defect-laden systems must satisfy the ASRs, and the difference must be adjusted so that it is strictly bounded within the area where the Green's function is calculated.

This formalism has been successfully applied to cases such as diamond [KCLM2014], GaN [KCW+2018] and highly doped Si [DCW+2020], always showing excellent predictive ability with no other input parameters than the defect concentration. The level of quantitative agreement is so high that relatively inexpensive thermal conductivity measurements can be used, in conjunction with these calculations, to determine the type and concentration of defects in a sample, as was done in [KCM2016], where it was revealed that Ni/vacancy antisites are the dominant scattering mechanism in thermoelectric ZrNiSn samples, solving a controversy between different experimental measurements. This stands in stark contrast with traditional approximations like the Klemens-Callaway model [AV1962], which rely on fitted parameters and can produce unphysical results. An example of the latter is that, for vacancies, where the magnitude of the mass perturbation $V_{\boldsymbol{M}}$ is completely irrelevant because the atom is disconnected from the lattice in the perturbed configuration, the Klemens-Callaway model still predicts nonzero scattering rates from that mass perturbation; meanwhile, the Green's function method yields the right result without

any adjustment. The availability of quantitative models has also revealed the existence of superscatterers such as B substitutions in SiC [KCD+2017]: those are defects that reduce the thermal conductivity of their host to a much larger degree than most other impurities at similar concentrations, by introducing strong resonances in frequency bands that are especially important for thermal transport.

The same methods can be used to study random alloys, modelled as an effective medium with a random distribution of substitutions that scatter phonons. Employing a single-site-averaged perturbation extracted from DFT calculations on special quasirandom structures representative of the alloy [ZWFB1990], quantitative agreement with experiment is achieved even for InAs/GaAs alloys, where there is significant structural distortion with respect to the parent compounds [ACMM2018].

Extending the method to 1D defects involves treating one of the dimensions in reciprocal space and replacing the tetrahedron method by its 2D equivalent, the linear triangle method [AL1987]. This enabled the treatment of dislocations in GaN [WCMM2019], for which the structural deformation and the corresponding long-range IFC perturbation had to be modelled using a matched combination of an elastic deformation model and actual atomistic calculations.

On the whole, Green's-function-based methods for characterizing the effect of defects on phonon transport have proven themselves as a viable strategy to obtain predictive estimates without experimental input; however, their computational cost is significant, both because of the need to study the complex local relaxations around defects and because of the large number of DFT calculations on low-symmetry configurations that are required to obtain the IFC perturbation. Additionally, defects may exist in different charge states, and in a doped semiconductor mapping a measured charge-carrier density to an actual defect concentration is a decidedly nontrivial problem in computational thermodynamics [BGS+2015].

3.2 Interfaces and superlattices.

The most common kind of 2D defect is the sample boundary, which is present in every measurement. Boundaries are responsible for the characteristic low-temperature behavior of thermal conductivity curves, which go to zero as $T \to 0$: it can be shown that for an infinite sample κ_ℓ would diverge in that limit [Zim1960]. The same kind of result is obtained from a typical phonon BTE calculation of the kind outlined here, but only as a numerical

artifact due to the discretization of the BZ using a regular grid: proper integration and allowed process detection at lower temperatures would require much denser sampling close to the Γ point. Luckily, relatively simple approximations can account for the presence of a boundary with different geometries, like wires [LML+2012] and films [CVK+2017]. For a generic bulk system where the geometry of the boundary is unknown or not strictly relevant, the usual choice is to include an additional contribution to the scattering rates that reflects a mean free path of the order of the characteristic sample size L, with an expression $\tau^{-1}_{\lambda,\text{boundary}} = |\boldsymbol{v}_\lambda|/(FL)$ for a suitable form factor F. This can be justified heuristically, as an estimate of the average distance between boundary scattering events. Its main downside is that F often needs to be treated as a fitting parameter, breaking the parameter-free nature of the approach at low temperatures.

Interfaces between media, on the other hand, are some of the more complex defects from the perspective of phonon transport. In the directions parallel to the surface there are often reconstructions that break the periodicity of the bulk, while in the perpendicular direction other phenomena like interdiffusion, polarity and composition gradients create very involved atomistic configurations. Insofar as those configurations can be determined, they can be modelled in detail and their effect on phonons computed employing Green's functions, albeit using quite specific techniques. A good synthesis can be found in [Ong2018]; a crucial part is the realization that a periodicity still exists in the directions parallel to the surface, even if it is different from that of the bulk, so a parallel wave vector $\boldsymbol{q}_\parallel$ can be defined that is conserved in interface scattering processes. Therefore, the problem can solved individually for each $\boldsymbol{q}_\parallel$, and is decoupled into a set of effective 1D phonon transmission calculations with a typical Landauer-Büttiker setup, illustrated in Fig. 3. Reconstruction is assumed to be confined to a finite region around the interface, the scattering region, beyond which the system maintains its bulk structure and is therefore translationally symmetric in the direction perpendicular to the interface. Each of the sides of the interface, acting as a lead, is split into blocks thick enough that interblock IFCs can be neglected beyond the first neighbors, and hence each lead is characterized by a pair of "on-site" and "hopping" IFC blocks, by analogy with a 1D electronic tight-binding problem. Each of the leads is also connected to the scattering region through another IFC block, and that region has its own "on-site" term, but there is no direct connection between the leads (which can be accomplished by taking a large enough scattering region). The Green's functions of the uncoupled leads are

obtained from the corresponding blocks using a real-space technique known as decimation [GTFL1983; ZFM2007], an iterative process that starts by constructing a small version of the lead and doubles the size of that construction in each iteration. From there, two self-energies can be defined and finally the Green's function of the coupled system in the central region is readily recovered. That allows the total phonon transmission at a given frequency to be extracted from the usual Caroli formula; however, it is often more useful to obtain the mode-to-mode transmissions from the left to the right lead across the interface, which are encoded in the so-called Bloch matrices [Ong2018]. Through this formalism, the fine details of phonon transmission across precisely characterized interfaces, such as phase and twin boundaries in group-IV and III-V semiconductors, can be recovered [CLR+2019]. Once more, this contrasts with traditional simplified models, in this case the acoustic-mismatch and diffuse-mismatch models [RCM2005], which rely on very crude hypotheses about how phonons are reemitted and ignore most of the characteristics of those phonons; particularly noteworthy are the effects of polarization, evident in the different behavior of transverse and longitudinal modes at those phase and twin boundaries.

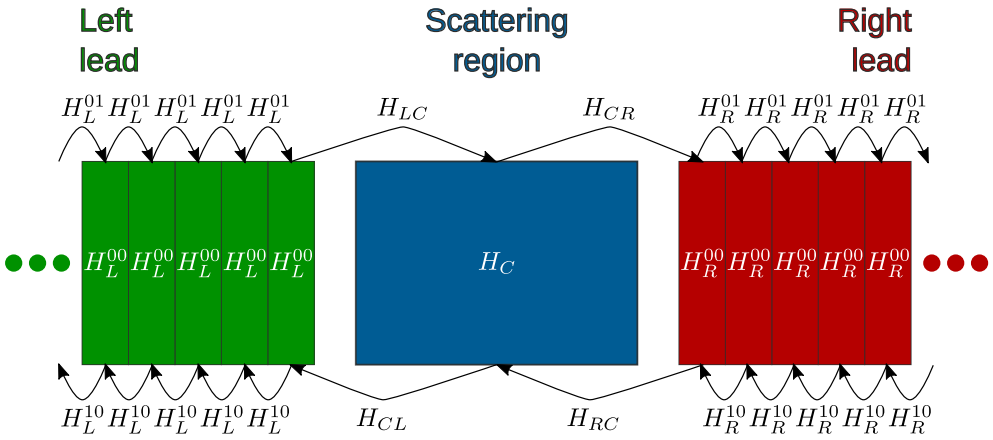

Figure 3: Diagram of the partition of the harmonic IFC matrix in blocks used for calculating the phonon transmission across an interface.

Directly connected to the problem of a single interface is the study of binary superlattices, structures with a periodic composition profile along the growth axis. Superlattices are highly tunable through modifications to that profile, and their physical properties are not determined by their net composition, making them very attractive from a technological standpoint. As an example, Si/Ge superlattices with a reduced Ge concentration can be designed to have a thermal conductivity as low or lower than the random Si/Ge allows used

in thermoelectric products [CKF+2013]; this is very interesting because most of the cost of the alloy is driven by that germanium content. That kind of behavior can be reproduced quantitatively if the superlattice is modelled as an effective medium on top of which two different perturbations are imposed, one due to the composition profile along the growth direction (the barrier component) and the other caused by chemical disorder in the two perpendicular directions (the alloy component). The former, a significant perturbation, must be treated using Green's functions, while the latter can be handled with a slightly adapted version of Tamura's perturbative formula for isotopes. This has been shown to provide excellent agreement with measurements when paired with a thermodynamic model of superlattice growth, for instance in the cases of Ge/Si [TCV+2018] and InAs/GaAs [CVT+2018] superlattices, to the point that a profile can be designed to target a particular thermal conductivity that is later confirmed after its synthesis and measurement. Figure 4 shown some examples for InAs/GaAs superlattices. A special integration method had to be devised to obtain the Green's function for this application, since the linear tetrahedron method exhibits poor behavior when extrapolated to 1D. Using cubic (instead of linear) interpolation for each phonon band within each segment of the 1D BZ fixes the problem without compromising the analytic integration. To determine the coefficients a cubic polynomial, the phonon group velocities must be used in the interpolation, in addition to the angular frequencies; as a beneficial side effect, the approximation is satisfactory over longer segments and therefore sparser grids can be used.

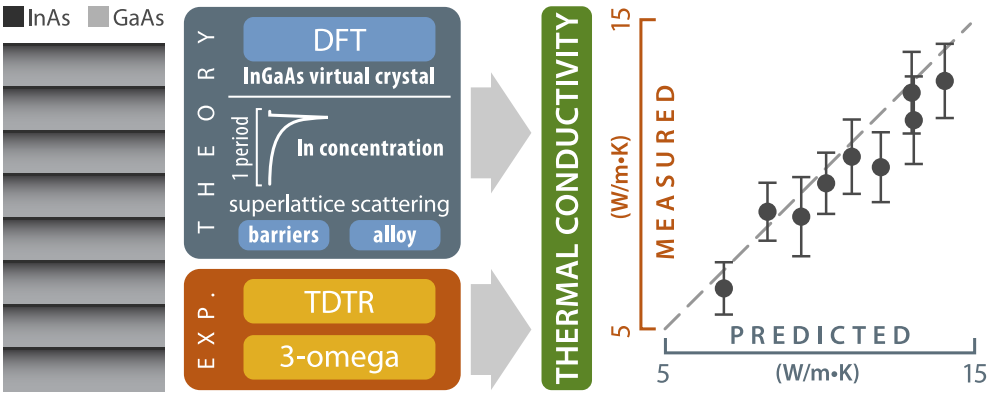

Figure 4: Schematic representation of the calculation and measurement workflow for InAs/GaAs superlattices, and comparison between calculations and experiment. Reproduced with permission from [TCV+2018].

3.3 Subperiodic systems.

In the last decades, nanosystems have risen to prominence because of their seemingly infinite versatility in manifesting new physical phenomena and the tunability of their properties for technological applications. The field of thermal transport is no exception to this trend: silicon nitride nanostructures were used to measure the quantum of thermal conductance [SHWR2000], Si nanowires with rough boundaries have been proposed as candidates for ultralow thermal conductivities [HCD+2008] and graphene may have the highest thermal conductivity of any known material, in competition only with diamond [PVR2012].

Quasi-2D monolayers and multilayers have been tackled very successfully using the BTE formalism outlined, both in pristine form [LLC+2014] and in the presence of defects [MCI+2024]. Nevertheless, special care must be exercised when computing their phonon spectra, since the effect of the symmetries of free space is different in each dimensionality. Specifically, the phonon spectrum any quasi-2D crystalline system — not just monolayers, but any system that is only periodic in two dimensions — must possess a quadratic branch with zero group velocity around the Γ point, corresponding to vibrations perpendicular to the plane of periodicity [CLL+2016]. This is a requirement of continuous rotational invariance, resulting in a second set of ASRs that do not have a direct effect on the spectra of 3D systems [GW1966]. Those ASRs need to be enforced on the raw IFCs obtained from DFT, which typically violate them by large margins. It is also necessary for consistency with elasticity theory in the long-wavelength limit, since one of the branches of Lamb waves in vibrating membranes is indeed predicted to have a quadratic dispersion curve [LLKP1986]. Unfortunately, the literature is full of proposed phonon spectra for 2D systems that show the effects of such violations: either nonzero group velocities at Γ or a characteristic "pocket" of imaginary frequencies in the branch that should be quadratic, placed between Γ and the first commensurate $\boldsymbol{q}$ in a given direction (e.g. [FZKS2015; JM2015; MKS2014; XHB2014], among dozens of other published studies). The effects on the calculated conductivity can be catastrophic, as shown in [CLL+2016] and in figure 5, where the numerical artifacts introduced by the neglect of symmetry cause errors of more than 100% and the reversal of the predicted anisotropy.

The situation with quasi-1D structures, such as nanotubes and nanowires, is more nuanced. On the one hand, large-diameter nanowires can be treated as a bounded sample of a bulk material with a suitable boundary scattering term [LML+2012]. On the other hand,

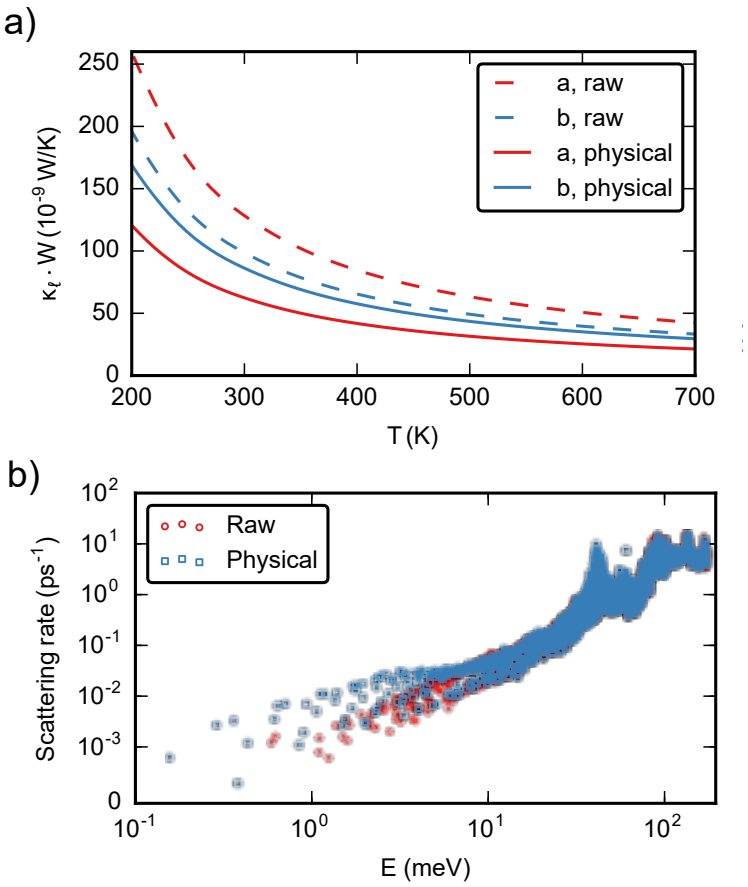

Figure 5: 2D thermal conductivity (a) and three-phonon scattering rates (b) in borophene, with a quasi-2D Pmmn structure, computed using IFCs from DFT fulfilling only the translational ASRs ("raw") or the full set of translational and rotational ASRs ("physical"). Reproduced from [CLL+2016], published under an open access CC-BY-4.0 license.

narrow quasi-1D nanostructures require explicit calculations of their phonon spectra, which is fraught with problems. First, the effect of rotational ASRs is even more marked than in 2D: they must be fulfilled so that the phonon spectrum contains four acoustic branches (instead of three), two of which must be quadratic. Second, the detection and handling of discrete symmetries is also a challenge. When only translations along the periodic axis are taken into account, the unit cell required to generate an infinite nanowire or nanotube contains a very large number of atoms, and accordingly the number of phonon bands is extremely large. As a matter of fact, the right kind of symmetry group to deal with these structures are not space groups but line groups [DM2010], combining generalized translations (including screw operations and glide planes) with axial point groups that are not

subject to the crystallographic restriction theorem and can therefore contain rotations of any order. Studying the vibrational modes of a nanowire or nanotube in terms of the irreducible representations of its line group not only enables the use of a much smaller motif (the so-called symcell), but also yields new quantum numbers to classify the phonon branches according to how they behave under rotations and reflections, analogously to how $\boldsymbol{q}$ characterizes the behavior of a each mode under translation [CNM2019]. The combined effect of neglecting the rotational ASRs and not using the full line group creates a host of numerical artifacts, detailed in figure. 6, that make the phonon spectrum unusable for further calculations. Unfortunately, most of the relevant software packages target 3D crystals and only implement space groups, and awareness about line groups among the community is very limited.

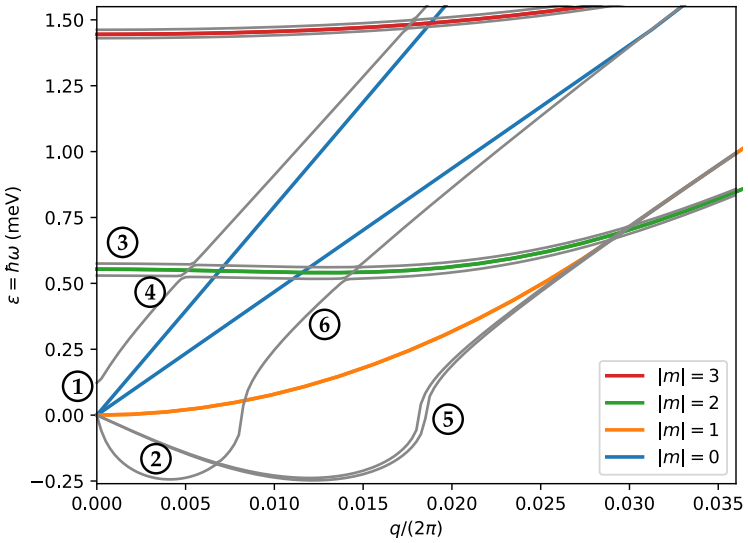

Figure 6: Common artifacts derived from treating phonons in quasi-1D structures using a 3D formalism, in the example of an MoS_2 nanotube: (1) wrong number of acoustic branches; (2) imaginary frequencies; (3) spurious breakdown of degeneracies; (4) misprediction of band crossings; (5) finite group velocities in branches that should be quadratic; (6) errors in the speed of sound. Reproduced from [CNM2019], published under an open-access CC-BY-3.0 license.

Regarding phonon scattering and thermal transport, the elastic transmission across several kinds of defects in quasi-1D settings has been studied from first principles [CGVM2011; MSBS2008] using the same Green's function formalism introduced for interfaces in the previous section (with the parallel component of $\boldsymbol{q}$ restricted to zero). However, the BTE formalism in the form explained so far is normally not applicable in this context because

of the high degree of anharmonicity. A rigorous treatment requires the use of anharmonic Green's functions, whose the formalism is known [GZB+2021] but for which no general implementation is in widespread use because of their high cost. Hence, alternative approaches using molecular dynamics [CLR+2019] or Green-Kubo-based methods [ZLL2016] are more often found in the literature when anharmonicity must be explicitly included.

3.4 Simulating time-dependent processes in structured systems.

Motivated by the success of the BTE in treating steady-state lattice thermal transport in pristine and defect-laden crystalline materials, it is natural to wonder whether the formalism can be extended to simulate whole devices, containing regions with different materials and specific geometries. Moreover, for maximum usefulness those simulations should encompass time-dependent processes as well.

In this more general setting, one must go back to the phonon BTE in the form of Eq. (8) and the non-linearized form of the scattering operator in Eq. (17) (plus the relevant contributions from elastic scattering). Unfortunately, this is a large set of partial differential equations formulated over six spatial dimensions (three for $\boldsymbol{r}$ and three for $\boldsymbol{q}$) and over time, and thus runs into the so-called curse of dimensionality, whereby any attempt at a direct solution through the use of basis sets or a discrete grid scales very poorly. Although Monte Carlo (MC) methods are broadly applicable in such situations, MC simulations using phonons as particles have traditionally generated subpar outcomes. The reason is twofold: first, it is very hard to fulfill the conservation of energy in a context where the number of phonons is not conserved; second, the vast majority of the computational effort is wasted on modelling the equilibrium component of the distribution, which does not make any contribution to thermal transport. An alternative approach is energy-based variance-reduced MC (VRMC) [JN2012; PH2011], which deals with the deviation of the local energy distribution with respect to equilibrium at a reference temperature (T_{ref}): $g_\lambda(\boldsymbol{r},t) \coloneqq \hbar\omega_\lambda[f_\lambda(\boldsymbol{r},t) - f_{\text{BE},\lambda}(T_{\text{ref}})]$. That deviational distribution is then split into a fixed number, N_{part}, of samples or "particles":

$$g_\lambda(\boldsymbol{r},t) \simeq E_{\text{eff}} \sum_{p=1}^{N_{\text{part}}} \delta^3[\boldsymbol{r} - \boldsymbol{r}_p(t)]\delta^3[\boldsymbol{q} - \boldsymbol{q}_p]\delta_{\boxdot,\boxdot_p}. \tag{28}$$

Each of these particles has a well defined position and is associated to a phonon branch $\lambda \equiv (\boldsymbol{q}, \boxdot)$, but they represent packets of energy in one mode instead of phonons. By explicitly using $f_{\mathrm{BE},\lambda}(T_{\mathrm{ref}})$ as a reference by using particles whose number is conserved, VRMC avoids both classes of problems from ordinary phonon-based MC.

A particularly efficient implementation of the VRMC can be achieved under the RTA [PLH2014], since a regime can be defined where each deviational particle can be treated independently, and therefore the algorithm can be parallelized. Based on the physics of phonons, deviational particles are emitted and absorbed at isothermal reservoirs and temperature gradients, experience intrinsic scattering in bulk regions (including inelastic scattering with a change of frequency) and are reflected or transmitted at interfaces.

The public, open source version `almaBTE` package, which I coauthored and maintain [CVK+2017], implements this form of VRMC for the efficient and accurate simulation of structured systems. It also implements specific models for treating thin films, superlattices, alloys and transient phenomena in bulk systems, and contains a more advanced version of the capabilities of `ShengBTE`. Additional code implements the Green's functions methods for point defects and interfaces discussed in previous sections.

The computational cost of ab-initio VRMC in a full-BTE setting is much higher, due to the loss of the much simpler RTA form of the scattering operator. The formalism was introduced by Landon and Hadjiconstantinou in [LH2014], but using a low-performance scaling-and-squaring method to compute the large matrix exponential involved in the calculation of the propagator. `BTE-Barna` [RCC2022], an extension of `almaBTE` focusing on 2D materials, improves upon that original implementation by using a Krylov-subspace approach much better suited for the problem, along with an interpolation of the propagator for systems with multiple reference temperatures. The results show clear departures from the RTA in systems such as phosphorene nanoribbons, not only in the details of the phonon populations and the thermal flux, but in the effective thermal conductivity as well. This implementation opens the door to simulating phenomena, like second sound [HDC+2019], which are explicitly beyond the reach of the RTA. Figure 7 shows steady-state results for a three-terminal borophene device computed with `BTE-Barna`.

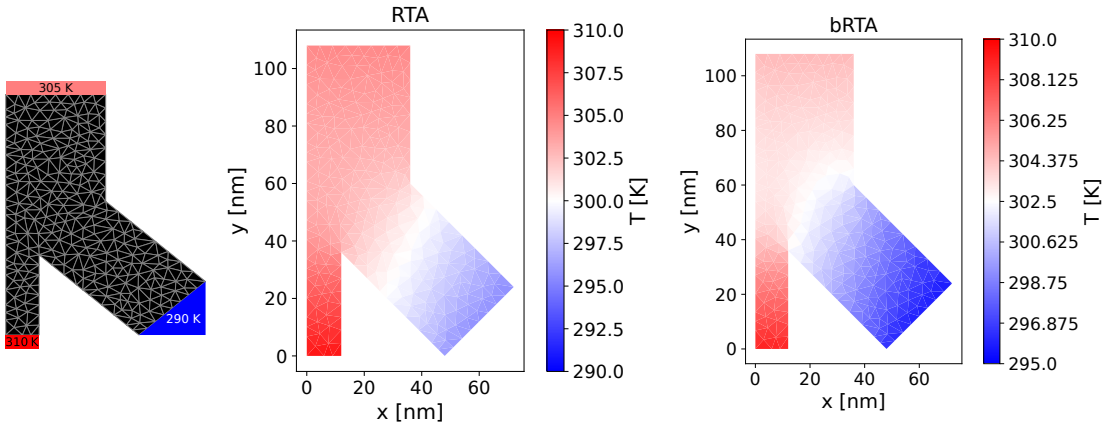

Figure 7: `BTE-Barna` prediction of the steady-state temperature distribution in a three-terminal structure made out of borophene, computed using VRMC. Left: boundary conditions and spatial grid used to gather deviational particle statistics. Center: RTA solution. Right: full-BTE solution. Adapted from [RCC2022], published under an open-access CC-BY-4.0 license.

3.5 Beyond three-phonon processes.

The truncation of Eq. (10) at the third order is physically justifiable, but also born out of necessity, since the treatment of higher-order anharmonicity is computationally very expensive. However, situations exist where four-phonon processes cannot be ignored, either because the temperature is high enough or because three-phonon scattering is relatively weak. While one of the obstacles, namely the calculation of high-order IFCs, has been alleviated by the development of regression-based approaches and user-friendly software like `hiPhive` [EFE2019], the computational complexity of the detection of four-phonon processes and the calculation of their matrix elements remains a challenge, so far palliated mainly by the availability of more powerful computers. Packages like `FourPhonon` [HYL+2022], an extension of `ShengBTE` take care of harnessing the symmetries, running the calculations and solving the BTE, although in practice calculations must normally use a much sparser grid than for the third-order part. As more BTE solutions including higher order anharmonicity become available, the awareness about their importance in materials with extreme thermal behavior grows [LLWX2025]: for example, they are key in describing the ultrahigh thermal conductivity of θ-phase TaN, a semimetal whose thermal transport is dominated by phonons [KYM+2021].

One of the clear signs that the description of thermal transport in a material must

go beyond three-phonon processes comes from the high-temperature behavior of its $\kappa_\ell(T)$ curve, which is characteristically $\propto T^{-1}$ for third-order anharmonicity. While including the four-phonon contribution changes this dependence, in very strongly anharmonic materials $\kappa_\ell(T)$ does not decrease with temperature at all, but instead shows a plateau. This behavior is very characteristic of crystals with very complex unit cells and of amorphous materials, and reproducing it requires going beyond a phonon-based formalism. The first semiquantitative treatment of this was the Allen-Feldman theory [AFFW1999], which classifies normal modes into propagons (extended and propagating), diffusons (extended but nonpropagating) and locons (localized). In a strongly anharmonic system where the scattering rates increase with frequency, the so-called Ioffe-Regel crossover, at which the lifetime of vibrations becomes shorter than half of their oscillation period, marks the threshold between propagons and diffusons. Heat transfer by diffusons depends on their diffusivity and cannot be treated with the BTE in the form seen so far. A modern unified theory was proposed in 2019 by Simoncelli et al. [SMM2019b], with explicit expressions for the diffuson contribution that can be computed ab initio. The diffusivity is related to the off-diagonal elements of the same group velocity operator appearing in Eq. (14).

3.6 Temperature-dependent IFCs.

There are some situations in which the Taylor expansion of the potential energy in Eq. (10), which is intrinsically semilocal, is not a useful description of the energy landscape sampled by the system, but in which most of the associated formalism can still be applied if a different, more suitable effective harmonic approximation to their potential energy can be devised. This is useful, in particular, for two classes of systems: those crystals whose strong anharmonicity lead to temperature-dependent effective phonon bands, and some phases that are mechanically unstable below a certain temperature, and which therefore contain imaginary frequencies in their basic harmonic spectrum.

There are several different strategies to obtain such an effective harmonic potential, such as the temperature-dependent effective potential (TDEP) method [HAS2011], which uses samples from finite-temperature molecular dynamics trajectories, or the stochastic self-consistent harmonic approximation (SSCHA) [ECM2013], based on the minimization of a rigorous upper bound to the free energy of the system. On a practical level, all of them aim to achieve some degree of self-consistency between the configurations visited by

the system at a given temperature according to the effective potential and the energy and forces in those configurations. This is perhaps most explicit in the quantum self-consistent ab-initio lattice dynamics (QSCAILD) method [vCM2021]: starting from a version of the basic harmonic spectrum with the imaginary frequencies removed, it proceeds iteratively by generating a set of samples from the real-space probability density of atomic displacements predicted by quantum statistical mechanics, computing the forces on atoms in each of those configurations with DFT, and fitting a new potential based on those results, until convergence is achieved. QSCAILD has shown its capabilities in scenarios such as a high-throughput exploration of a set of about 400 oxide and fluoride perovskites [vCO+2016], including the detection of those that become cubic at finite temperature and an accurate calculation of their thermal conductivities, or the exploration of the complicated phase diagram of hafnia [BCNM2022]. Figure 8 shows the effective spectrum of cubic hafnia predicted in that reference, and specifically its evolution from unstable to stable at increased temperatures. All of those methods have in common that they require a significantly higher number of DFT calculations; therefore, strategies like importance sampling that enable the reuse of samples are very helpful in those contexts [BCNM2022]. Even beyond these extreme examples, it has been shown that temperature-dependent changes in the phonon spectrum can have a material impact on the predicted thermal conductivity of a variety of systems [LLWX2025].

3.7 Accelerated calculation of IFCs.

A common feature of all the discussed presented in this section is their high computational cost, even compared to the already expensive basic BTE solution for pristine bulk crystals in the steady state presented earlier. Broadly speaking, that cost can be traced to the need to compute more IFCs or higher-order ones, which in turn translates into more or larger DFT calculations. Therefore, techniques that bypass or speed up those calculations can deliver important quantitative advances in terms of the number or complexity of systems that can be treated. This subsection will discuss a sample of such techniques, all emerging from the field of machine learning that is currently having a tremendous impact on materials science, as well as so many other areas of society.

The first example consists in exploiting the regularities among the IFCs of crystals with the same structure but different chemical compositions. While this has been known by

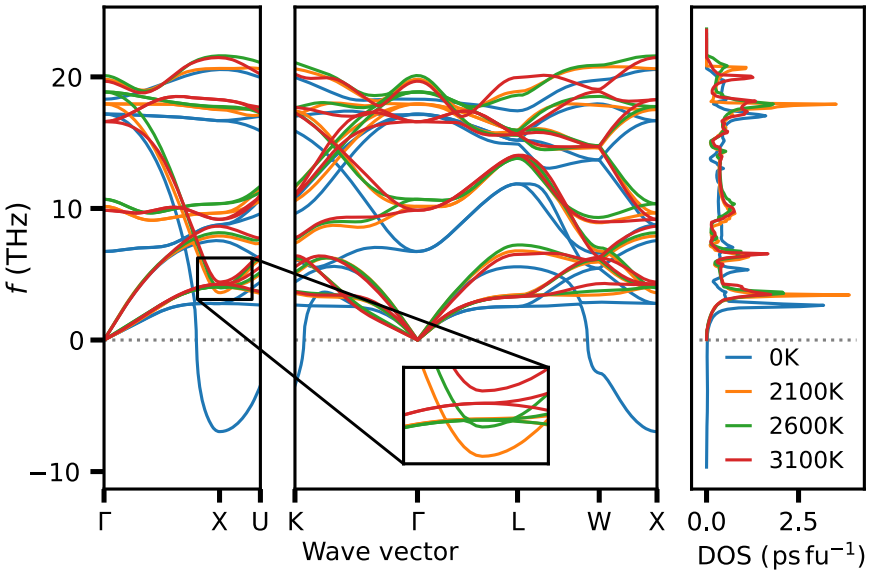

Figure 8: Temperature dependence of the computed effective phonon spectrum of hafnia, showing how that phase reaches mechanical stability. Reproduced from [BCNM2022], published under an open-access CC-BY-NC-4.0 license.

the community for a long time in particularly simple cases (e.g., computing the phonon spectrum of Ge with the harmonic IFCs of Si, and just changing the masses, yields quite a good result [GZB+2021]), modern regression techniques make it exploitable in more general settings. In [CLM+2014], a library formed by the approximately 80000 half Heuslers that could theoretically be built out of the non-radioactive elements of the periodic table is screened in search of promising candidates for thermoelectric applications. After filtering by criteria of mechanical and thermodynamical stability, and keeping only the semiconductors in the set, 75 candidates are left whose thermal conductivity must be obtained. To avoid explicitly calculating all the required anharmonic IFCs, a multiple multivariate linear regression model is built based on a smaller training set. The model exploits approximate linear dependencies between third-order IFCs, and results in a method to reconstruct the full third-order IFC tensor using just four constants as input, while respecting all the symmetries. The result has high predictive power, and was in fact even able to detect an outlier among the "exact" results that was later revealed to contain an error. By using this construction, the number of DFT calculations per compound is reduced from 344 to 16.

At the other end of the spectrum, a regression model can be created to predict the IFCs of compounds with the same chemical composition but different structure, i.e., of

polymorphs. In [LvRC+2018], this idea was applied to 121 non-equivalent mechanically stable minima of $KZnF_3$. Specifically, we used a random-forest regression [Bre2001] with equivariant inputs to predict the harmonic IFC tensors, with very good results for thermodynamic quantities at the quasiharmonic level and even for quantitative features of the IFCs themselves.

By far the most flexible and revolutionary contribution to the field from machine learning, however, is the development of machine-learning interatomic potentials (MLIP), advanced regression models that can model the dynamics of an atomistic system with ab-initio-like quality but at a cost similar to a classical potential. That area of research has exploded in the past decade, and it would be impossible to to present even a small survey of architectures here, so the reader is instead referred to a dedicated review [LZLS2025]. Suffice it to say that at the core of a MLIP is a machine-learning model, most often a kind of neural network, typically implemented on top of a modern framework like `Pytorch` [PGM+2019] or `JAX` [BFH+2018]. A key feature of those frameworks is the fact that they implement high-performance automatic differentiation [BPRS2017], i.e, the propagation of derivatives through a tree of elementary operations using systematic implementations of the chain rule. For instance, JAX implements both of the major modes of automatic differentiation, the forward and reverse modes, whose results are, respectively, a Jacobian-vector-product operator and a vector-Jacobian-product (VJP) operator. A single application of the VJP is enough to extract all the components of the gradient of a scalar-valued multivariate function (such as when extracting the forces on all atoms from the potential energy) at a cost comparable to that of evaluating the function itself, with a high degree of accuracy and almost negligible implementation effort. This marks a huge deviation from the traditional process of potential development when it comes to, e.g., making minimization algorithms or molecular dynamics possible; however, for IFC calculations the implications of automatic differentiation are much more extensive. The whole set of second-order IFCs can be obtained as a Jacobian of a gradient (forward mode composed over reverse mode); alternatively, the dynamical matrix at a $\boldsymbol{q}$ point can be evaluated from a JVP of a JVP and obtained without passing through the IFCs at all, and even the derivative of that dynamical matrix with respect to volume is readily accessible if that kind of anharmonic information is desired. Similarly, a high-order Taylor-series form of the potential energy can be evaluated at a point without computing the IFCs involved — which would be impossible on account

of the geometric growth of their number with the maximum order of the series — through recursive applications of differential operators [BCM2023]. Automatic differentiation blurs the line between classical potentials and ab-initio techniques like DFPT, and is starting to be applied directly in the first-principles world as well to overcome the performance, correctness and cost problems of the direct implementation of derivatives [LSD+2024].

MLIPs are making a fundamental contribution to the study of complex systems for which a direct DFT approach is unfeasible, and their usefulness has been demonstrated, among other cases, for defect-laden quasi-1D [CWMC2025], quasi-2D [PCWM2024] and 3D [DSC+2025] structures. A promising development is the release of so-called "foundation models" [BBC+2023], pretrained over large libraries of materials or molecules, which can be used directly or refined for a particular application, drastically reducing, or even completely eliminating, the effort of generating DFT data to train a model from scratch.

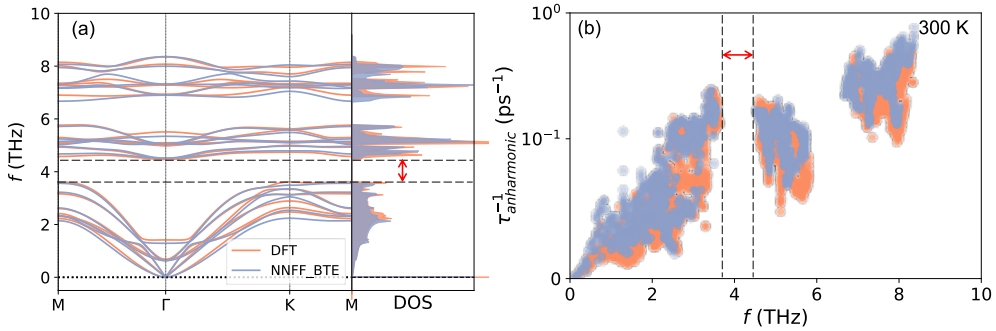

Figure 9: Comparison of the phonon spectrum and anharmonic phonon scattering rates of bilayer PtSTe calculated directly with DFT and through an MLIP based on NeuralIL [CMW+2023]. Reproduced from [PCWM2024], published under an open-access CC-BY-4.0 license.

4 Concluding remarks

Thermal transport is such an active field, with so many concurrent developments at different, but partially overlapping, levels of abstraction, that no single review can expect to cover but a small fraction of it. Nevertheless, I hope to have conveyed, at the very least, a message of optimism. After the first breakthroughs in computational solutions to the BTE with ab-initio dispersions, which shattered the traditional perspective that it was an unsolvable problem, progress has been remarkably fast, to the point that simulations of quite realistic models of devices are now possible. Not only have workable approximations

appeared for a large variety of phonon scattering mechanisms and combinations thereof that retain levels of predictive power similar to that of the first solvers for single crystals, but the software ecosystem has matured greatly to allow non-specialists to integrate this kind of research in more classes of studies. Examples of this are the increasing number of high-throughput screenings of thermal conductivities in different settings and the joint treatment of charge carrier and phonon transport from first principles. The next challenge, and one that has proven rather elusive so far despite some notable exceptions, is to make bigger inroads into industry, where a surprising amount of modelling is still done using finite-element solutions to the Fourier equation couple with other macroscopic differential equations.

Acknowledgments. I am honored and grateful to receive this prize from the Real Academia de Ciencias de Zaragoza and I extend my sincere thanks to its esteemed members for this recognition.

My work on ab-initio lattice thermal transport would not have been possible without the support of the incredibly talented teams I have been part of. The names of the people to which I owe a big debt of gratitude are too many to cite here, but I would be remiss if I did not mention my PhD advisors, Luis Miguel Varela and Luis Javier Gallego del Hoyo, the ShengBTE and almaBTE teams at CEA Grenoble and elsewhere, and all past and present members of Georg Madsen's group at TU Wien. Working with them has been the privilege and the honor of my lifetime. I am most deeply indebted to Natalio Mingo, a true scientific luminary whose intelligence and tireless creativity are behind many of the innovative techniques discussed in this review. His personality and work have left an indelible mark in me. May he rest in peace.

I cannot neglect to mention my colleagues and friends at INMA, whom I want to thank for creating a welcoming environment and broadening my scientific horizons.

Finally, I must also acknowledge grant PID2023-148359NB-C21 funded by MICIU/AEI /10.13039/501100011033 and the European Union FEDER, as well as all the funding I have received over the years from national and international institutions.

References

[AV1962] B. K. Agrawal and G. S. Verma, *Phys. Rev.*, vol. 126, pp. 24–29, 1962. DOI: 10.1103/PhysRev.126.24.

[AFFW1999] P. B. Allen, J. L. Feldman, J. Fabian, and F. Wooten, *Philos. Mag. B*, vol. 79, pp. 1715–1731, 1999.

[ACMM2018] M. Arrigoni, J. Carrete, N. Mingo, and G. K. H. Madsen, *Phys. Rev. B*, vol. 98, p. 115 205, 2018. DOI: 10.1103/PhysRevB.98.115205.

[AL1987] J. A. Ashraff and P. D. Loly, *J. Phys. C: Solid State Phys.*, vol. 20, p. 4823, 1987. DOI: 10.1088/0022-3719/20/29/017.

[AT2024] K. S. Atsushi Togo and I. Tanaka, *Sci. Technol. Adv. Mater., Meth.*, vol. 4, pp. 2 384 822–2 384 836, 2024. DOI: 10.1080/27660400.2024.2384822.

[BdGDG2001] S. Baroni, S. de Gironcoli, A. Dal Corso, and P. Giannozzi, *Rev. Mod. Phys.*, vol. 73, pp. 515–562, 2001. DOI: 10.1103/RevModPhys.73.515.

[BBC+2023] I. Batatia *et al.*, 2023. arXiv: 2401.00096 [physics.chem-ph].

[BPRS2017] A. G. Baydin, B. A. Pearlmutter, A. A. Radul, and J. M. Siskind, *J. Mach. Learn. Res.*, vol. 18, pp. 5595–5637, 2017. [Online]. Available: https://dl.acm.org/doi/abs/10.5555/3122009.3242010.

[BGS+2015] S. Bhattacharya, N. S. H. Gunda, R. Stern, S. Jacobs, R. Chmielowski, G. Dennler, and G. K. H. Madsen, *Phys. Chem. Chem. Phys.*, vol. 17, pp. 9161–9166, 2015. DOI: 10.1039/C4CP05991C.

[BCM2023] S. Bichelmaier, J. Carrete, and G. K. H. Madsen, *Int. J. Quantum Chem.*, vol. 123, 2023. DOI: 10.1002/qua.27095.

[BCNM2022] S. Bichelmaier, J. Carrete, M. Nelhiebel, and G. K. H. Madsen, *Phys. Status Solidi RRL*, vol. 16, p. 2 100 642, 2022. DOI: 10.1002/pssr.202100642.

[Blö1994] P. E. Blöchl, *Phys. Rev. B*, vol. 50, p. 17 953, 1994. DOI: 10.1103/PhysRevB.50.17953.

[Bol1872] L. Boltzmann, *Sitzungsber. Kaiserl. Akad. Wiss., Math.-Naturwiss. Cl.*, vol. 66, pp. 275–370, 1872.

[BUBC1959] R. Bowers, R. Ure Jr, J. Bauerle, and A. Cornish, *J. Appl. Phys.*, vol. 30, pp. 930–934, 1959. DOI: 10.1063/1.1735264.

[BFH+2018] J. Bradbury *et al.*, *JAX: Composable transformations of Python+NumPy programs*, version 0.3.13, 2018. [Online]. Available: http://github.com/google/jax.

[Bre2001] L. Breiman, *Mach. Learn.*, vol. 45, pp. 5–32, 2001. DOI: 10.1023/a:1010933404324.

[BMB+2007] D. A. Broido, M. Malorny, G. Birner, N. Mingo, and D. A. Stewart, *Appl. Phys. Lett.*, vol. 91, p. 231 922, 2007. DOI: 10.1063/1.2822891.

[Cal1959] J. Callaway, *Phys. Rev.*, vol. 113, pp. 1046–1051, 1959. DOI: 10.1103/PhysRev.113.1046.

[CGVM2011] J. Carrete, L. J. Gallego, L. M. Varela, and N. Mingo, *Phys. Rev. B*, vol. 84, 2011. DOI: 10.1103/physrevb.84.075403.

[CVT+2018] J. Carrete, B. Vermeersch, L. Thumfart, R. R. Kakodkar, G. Trevisi, P. Frigeri, L. Seravalli, J. P. Feser, A. Rastelli, and N. Mingo, *J. Phys. Chem. C*, vol. 122, pp. 4054–4062, 2018. DOI: 10.1021/acs.jpcc.7b11133.

[CLL+2016] J. Carrete, W. Li, L. Lindsay, D. A. Broido, L. J. Gallego, and N. Mingo, *Mater. Res. Lett.*, vol. 4, pp. 204–211, 2016. DOI: 10.1080/21663831.2016.1174163.

[CLM+2014] J. Carrete, W. Li, N. Mingo, S. Wang, and S. Curtarolo, *Phys. Rev. X*, vol. 4, p. 011 019, 2014. DOI: 10.1103/PhysRevX.4.011019.

[CLR+2019] J. Carrete, M. López-Suárez, M. Raya-Moreno, A. S. Bochkarev, M. Royo, G. K. H. Madsen, X. Cartoixà, N. Mingo, and R. Rurali, *Nanoscale*, vol. 11, pp. 16 007–16 016, 2019. DOI: 10.1039/c9nr05274g.

[CMW+2023] J. Carrete, H. Montes-Campos, R. Wanzenböck, E. Heid, and G. K. H. Madsen, *J. Chem. Phys.*, vol. 158, p. 204 801, 2023. DOI: 10.1063/5.0146905.

[CNM2019] J. Carrete, V. Ngoc Tuoc, and G. K. H. Madsen, *Phys. Chem. Chem. Phys.*, vol. 21, pp. 5215–5223, 2019. DOI: 10.1039/c9cp00052f.

[CVK+2017] J. Carrete, B. Vermeersch, A. Katre, A. van Roekeghem, T. Wang, G. K. Madsen, and N. Mingo, *Comput. Phys. Commun.*, vol. 220, pp. 351–362, 2017. DOI: 10.1016/j.cpc.2017.06.023.

[CWMC2025] Y.-J. Cen, S. Wieser, G. K. H. Madsen, and J. Carrete, *Ab-initio heat transport in defect-laden quasi-1d systems from a symmetry-adapted perspective*, 2025. arXiv: 2508.06882 [cond-mat.mtrl-sci]. [Online]. Available: https://arxiv.org/abs/2508.06882.

[CKF+2013] P. Chen, N. A. Katcho, J. P. Feser, W. Li, M. Glaser, O. G. Schmidt, D. G. Cahill, N. Mingo, and A. Rastelli, *Phys. Rev. Lett.*, vol. 111, p. 115 901, 2013. DOI: 10.1103/PhysRevLett.111.115901.

[CXH+2023] A. Chu, X. Xie, C. M. Hermann, W. Stork, and J. Roth-Stielow, "Towards predictive lifetime-oriented temperature control of power electronics in e-vehicles via reinforcement learning," in *2023 IEEE International Conference on Big Data (BigData)*, 2023, pp. 1667–1676. DOI: 10.1109/BigData59044.2023.10386292.

[DM2010] M. Damnjanovic and I. Milosevic, *Line Groups in Physics: Theory and Applications to Nanotubes and Polymers*. Springer, 2010, ISBN: 9783642111716.

[DS2025] S. Das and U. Sen, *Maximum entropy principle for quantum processes*, 2025. arXiv: 2506.24079 [quant-ph].

[DCW+2020] B. Dongre, J. Carrete, S. Wen, J. Ma, W. Li, N. Mingo, and G. K. H. Madsen, *J. Mater. Chem. A*, vol. 8, pp. 1273–1278, 2020. DOI: 10.1039/c9ta11424f.

[DSC+2025] Y. Dou, K. Shimizu, J. Carrete, H. Fujioka, and S. Watanabe, *Phys. Rev. Mater.*, vol. 9, p. 034 601, 2025. DOI: 10.1103/PhysRevMaterials.9.034601.

[Eco2006] E. N. Economou, *Green's Functions in Quantum Physics*, 3rd ed. Springer, 2006.

[EFE2019] F. Eriksson, E. Fransson, and P. Erhart, *Adv. Theory Simul.*, vol. 2, p. 1 800 184, 2019. DOI: 10.1002/adts.201800184.

[ECM2013] I. Errea, M. Calandra, and F. Mauri, *Phys. Rev. Lett.*, vol. 111, 2013. DOI: 10.1103/physrevlett.111.177002.

[Eye2012] V. Eyert, *The Augmented Spherical Wave Method: A Comprehensive Treatment*. Springer, 2012, ISBN: 978-3-642-25864-0.

[FZKS2015] X. Fan, W. T. Zheng, J.-L. Kuo, and D. J. Singh, *J. Phys.: Cond. Matter*, vol. 27, p. 105 401, 2015. DOI: 10.1088/0953-8984/27/10/105401.

[Fei2010] P. J. Feibelman, *Top. Catal.*, vol. 53, pp. 417–422, 2010. DOI: 10.1007/s11244-010-9451-6.

[Fou1822] J. B. J. Fourier, *Théorie Analytique de la Chaleur*. Didot, 1822, ISBN: 9780486495316.

[GHK+2006] M. Gajdoš, K. Hummer, G. Kresse, J. Furthmüller, and F. Bechstedt, *Phys. Rev. B*, vol. 73, p. 045 112, 2006. DOI: 10.1103/PhysRevB.73.045112.

[GW1966] D. C. Gazis and R. F. Wallis, *Phys. Rev.*, vol. 151, pp. 578–580, 1966. DOI: 10.1103/physrev.151.578.

[GBB+2009] P. Giannozzi *et al.*, *J. Phys. Condens. Matter*, vol. 21, p. 395 502, 2009. DOI: 10.1088/0953-8984/21/39/395502.

[GAB+2017] P. Giannozzi *et al.*, *J. Phys.: Condens. Matter*, vol. 29, p. 465 901, 2017. DOI: 10.1088/1361-648X/aa8f79.

[GAT1994] X. Gonze, D. C. Allan, and M. P. Teter, *Phys. Rev. B*, vol. 50, pp. 13 035–13 038, 1994. DOI: 10.1103/PhysRevB.50.13035.

[GL1997] X. Gonze and C. Lee, *Phys. Rev. B*, vol. 55, pp. 10 355–10 368, 1997. DOI: 10.1103/PhysRevB.55.10355.

[GTFL1983] F. Guinea, C. Tejedor, F. Flores, and E. Louis, *Phys. Rev. B*, vol. 28, pp. 4397–4402, 1983. DOI: 10.1103/PhysRevB.28.4397.

[GZB+2021] Y. Guo, Z. Zhang, M. Bescond, S. Xiong, M. Nomura, and S. Volz, *Phys. Rev. B*, vol. 103, 2021. DOI: 10.1103/physrevb.103.174306.

[HYL+2022] Z. Han, X. Yang, W. Li, T. Feng, and X. Ruan, *Comput. Phys. Commun.*, vol. 270, p. 108 179, 2022. DOI: 10.1016/j.cpc.2021.108179.

[HAS2011] O. Hellman, I. A. Abrikosov, and S. I. Simak, *Phys. Rev. B*, vol. 84, 2011. DOI: 10.1103/physrevb.84.180301.

[HCD+2008] A. I. Hochbaum, R. Chen, R. D. Delgado, W. Liang, E. C. Garnett, M. Najarian, A. Majumdar, and P. Yang, *Nature*, vol. 451, pp. 163–167, 2008. DOI: 10.1038/nature06381.

[HDC+2019] S. Huberman, R. A. Duncan, K. Chen, B. Song, V. Chiloyan, Z. Ding, A. A. Maznev, G. Chen, and K. A. Nelson, *Science*, vol. 364, pp. 375–379, 2019. DOI: 10.1126/science.aav3548.

[JN2012] J.-P. Peraud and N.G. Hadjiconstantinou, *Appl. Phys. Lett.*, vol. 101, p. 153 114, 2012. DOI: 10.1063/1.4942836.

[JM2015] A. Jain and A. J. McGaughey, *Sci. Rep.*, vol. 5, p. 8501, 2015. DOI: 10.1038/srep08501.

[KCLM2014] N. A. Katcho, J. Carrete, W. Li, and N. Mingo, *Phys. Rev. B*, vol. 90, p. 094 117, 2014. DOI: 10.1103/PhysRevB.90.094117.

[KCD+2017] A. Katre, J. Carrete, B. Dongre, G. K. H. Madsen, and N. Mingo, *Phys. Rev. Lett.*, vol. 119, 2017. DOI: 10.1103/PhysRevLett.119.075902.

[KCM2016] A. Katre, J. Carrete, and N. Mingo, *J. Mater. Chem. A*, vol. 4, pp. 15 940–15 944, 2016. DOI: 10.1039/C6TA05868J.

[KCW+2018] A. Katre, J. Carrete, T. Wang, G. K. H. Madsen, and N. Mingo, *Phys. Rev. Materials*, vol. 2, p. 050 602, 2018. DOI: 10.1103/PhysRevMaterials.2.050602.

[Koh1999] W. Kohn, *Rev. Mod. Phys.*, vol. 71, pp. 1253–1266, 1999. DOI: 10.1103/RevModPhys.71.1253.

[KF1996] G. Kresse and J. Furthmüller, *Phys. Rev. B*, vol. 54, pp. 11 169–11 186, 1996. DOI: 10.1103/PhysRevB.54.11169.

[KYM+2021] A. Kundu, X. Yang, J. Ma, T. Feng, J. Carrete, X. Ruan, G. K. H. Madsen, and W. Li, *Phys. Rev. Lett.*, vol. 126, p. 115 901, 2021. DOI: 10.1103/PhysRevLett.126.115901.

[LV1984] P. Lambin and J. P. Vigneron, *Phys. Rev. B*, vol. 29, pp. 3430–3437, 1984. DOI: 10.1103/PhysRevB.29.3430.

[LLKP1986] L. Landau, E. Lifshitz, A. Kosevich, and L. Pitaevskii, *Theory of Elasticity* (Course of Theoretical Physics). Butterworth-Heinemann, 1986, ISBN: 9780750626330.

[LH2014] C. D. Landon and N. G. Hadjiconstantinou, *J. Appl. Phys.*, vol. 116, p. 163 502, 2014. DOI: 10.1063/1.4898090.

[LA1972] G. Le Guillou and H. Albany, *Phys. Rev. B*, vol. 5, p. 2301, 1972. DOI: 10.1103/PhysRevB.5.2301.

[LvRC+2018] F. Legrain, A. van Roekeghem, S. Curtarolo, J. Carrete, G. K. H. Madsen, and N. Mingo, *J. Chem. Inf. Model.*, vol. 58, pp. 2460–2466, 2018. DOI: 10.1021/acs.jcim.8b00279.

[LGHC2025] S. Li, S. Guo, T. Hoke, and X. Chen, *Mater. Today Electron.*, vol. 12, p. 100 156, 2025. DOI: 10.1016/j.mtelec.2025.100156.

[LSD+2024] T. Li, Z. Shi, S. G. Dale, G. Vignale, and M. Lin, "Jrystal: A jax-based differentiable density functional theory framework for materials," in *Machine Learning and the Physical Sciences Workshop at NeurIPS 2024*, 2024.

[LCKM2014] W. Li, J. Carrete, N. A. Katcho, and N. Mingo, *Comput. Phys. Commun.*, vol. 185, pp. 1747–1758, 2014. DOI: 10.1016/j.cpc.2014.02.015.

[LML+2012] W. Li, N. Mingo, L. Lindsay, D. A. Broido, D. A. Stewart, and N. A. Katcho, *Phys. Rev. B*, vol. 85, p. 195 436, 2012. DOI: 10.1103/PhysRevB.85.195436.

[LZLS2025] Y. Li, X. Zhang, M. Liu, and L. Shen, *J. Mater. Inform.*, vol. 5, 2025. DOI: 10.20517/jmi.2025.17.

[LLWX2025] Z. Li, H. Lee, C. Wolverton, and Y. Xia, *High-throughput computational framework for lattice dynamics and thermal transport including high-order anharmonicity: An application to cubic and tetragonal inorganic compounds*, 2025. arXiv: 2507.11750 [cond-mat.mtrl-sci].

[LY1999] E. H. Lieb and J. Yngvason, *Phys. Rep.*, vol. 310, pp. 1–96, 1999. DOI: 10.1017/S0370-1573(98)00082-9.

[LLC+2014] L. Lindsay, W. Li, J. Carrete, N. Mingo, D. A. Broido, and T. L. Reinecke, *Phys. Rev. B*, vol. 89, 2014. DOI: 10.1103/physrevb.89.155426.

[MCI+2024] S. Mahendran, J. Carrete, A. Isacsson, G. K. H. Madsen, and P. Erhart, *J. Phys. Chem. C*, vol. 128, pp. 1709–1716, 2024. DOI: 10.1021/acs.jpcc.3c06820.

[MKS2014] A. Manjanath, V. Kumar, and A. K. Singh, *Phys. Chem. Chem. Phys.*, vol. 16, pp. 1667–1671, 2014. DOI: 10.1039/C3CP54655A.

[MW2014] A. A. Maznev and O. B. Wright, *Am. J. Phys.*, vol. 82, pp. 1062–1066, 2014. DOI: 10.1119/1.4892612.

[MSBS2008] N. Mingo, D. A. Stewart, D. A. Broido, and D. Srivastava, *Phys. Rev. B*, vol. 77, 2008. DOI: 10.1103/physrevb.77.033418.

[Nak2015] S. Nakamura, *Rev. Mod. Phys.*, vol. 87, pp. 1139–1143, 2015. DOI: 10.1103/RevModPhys.87.1139.

[OPG1972] A. Okhotin, A. Pushkarskij, and V. Gorbachev, *Thermophysical Properties of Semiconductors*. Atomizdat, 1972.

[OS1996] M. Omini and A. Sparavigna, *Phys. Rev. B*, vol. 53, pp. 9064–9069, 1996. DOI: 10.1103/PhysRevB.53.9064.

[Ong2018] Z.-Y. Ong, *J. Appl. Phys.*, vol. 124, p. 151 101, 2018. DOI: 10.1063/1.5048234.

[Ons1931] L. Onsager, *Phys. Rev.*, vol. 37, pp. 405–426, 1931. DOI: 10.1103/PhysRev.37.405.

[PCWM2024] L. Pan, J. Carrete, Z. Wang, and G. K. H. Madsen, *J. Phys. Chem. C*, vol. 128, pp. 11 024–11 032, 2024. DOI: 10.1021/acs.jpcc.4c02454.

[PLK1997] K. Parlinski, Z. Q. Li, and Y. Kawazoe, *Phys. Rev. Lett.*, vol. 78, pp. 4063–4066, 1997. DOI: 10.1103/PhysRevLett.78.4063.

[PY1989] R. G. Parr and W. Yang, *Density Functional Theory of Atoms and Molecules*. New York: Oxford University Press, 1989.

[PGM+2019] A. Paszke *et al.*, "PyTorch: An Imperative Style, High-Performance Deep Learning Library," in *Advances in Neural Information Processing Systems 32*, H. Wallach, H. Larochelle, A. Beygelzimer, F. d'Alché-Buc, E. Fox, and R. Garnett, Eds., Curran Associates, Inc., 2019, pp. 8024–8035. [Online]. Available: http://papers.neurips.cc/paper/9015-pytorch-an-imperative-style-high-performance-deep-learning-library.pdf.

[PML2013] L. Paulatto, F. Mauri, and M. Lazzeri, *Phys. Rev. B*, vol. 87, p. 214 303, 2013. DOI: 10.1103/PhysRevB.87.214303.

[Pei1929] R. Peierls, *Ann. Phys.*, vol. 395, pp. 1055–1101, 1929. DOI: 10.1002/andp.19293950803.

[PH2011] J.-P. M. Peraud and N. G. Hadjiconstantinou, *Phys. Rev. B*, vol. 84, p. 205 331, 2011. DOI: 10.1103/PhysRevB.84.205331.

[PLH2014] J.-P. M. Peraud, C. D. Landon, and N. G. Hadjiconstantinou, *Ann. Rev. of Heat Transf.*, vol. 17, pp. 205–265, 2014. DOI: 10.1615/AnnualRevHeatTransfer.2014007381.

[PVR2012] E. Pop, V. Varshney, and A. K. Roy, *MRS Bull.*, vol. 37, pp. 1273–1281, 2012. DOI: 10.1557/mrs.2012.203.

[RCC2022] M. Raya-Moreno, X. Cartoixà, and J. Carrete, *Comput. Phys. Commun.*, vol. 281, p. 108 504, 2022. DOI: 10.1016/j.cpc.2022.108504.

[RCM2005] P. Reddy, K. Castelino, and A. Majumdar, *Appl. Phys. Lett.*, vol. 87, 2005. DOI: 10.1063/1.2133890.

[Rei2016] L. E. Reichl, *A Modern Course in Statistical Physics*, 4th ed. Wiley-VCH, 2016, ISBN: 978-3-527-41349-2.

[SHWR2000] K. Schwab, E. A. Henriksen, J. M. Worlock, and M. L. Roukes, *Nature*, vol. 404, pp. 974–977, 2000. DOI: 10.1038/35010065.

[SMM2019a] M. Simoncelli, N. Marzari, and F. Mauri, *Nat. Phys.*, vol. 15, pp. 809–813, 2019. DOI: 10.1038/s41567-019-0520-x.

[SMM2019b] M. Simoncelli, N. Marzari, and F. Mauri, *Nature Phys.*, vol. 15, pp. 809–813, 2019. DOI: 10.1038/s41567-019-0520-x.

[Spa2012] N. A. Spaldin, *J. Solid State Chem.*, vol. 195, pp. 2–10, 2012. DOI: 10.1016/j.jssc.2012.05.010.

[TS1971] P. Tamarin and S. Shalyt, *Sov. Phys. Semiconductors*, vol. 5, pp. 1097–1098, 1971.

[Tam1983] S. Tamura, *Phys. Rev. B*, vol. 27, pp. 858–866, 1983. DOI: 10.1103/physrevb.27.858.

[TCV+2018] L. Thumfart, J. Carrete, B. Vermeersch, N. Ye, T. Truglas, J. Feser, H. Groiss, N. Mingo, and A. Rastelli, *J. Phys. D: Appl. Phys.*, vol. 51, p. 014 001, 2018. DOI: 10.1088/1361-6463/aa98c5.

[TT2015] A. Togo and I. Tanaka, *Scr. Mater.*, vol. 108, pp. 1–5, 2015. DOI: 10.1016/j.scriptamat.2015.07.021.

[vCM2021] A. van Roekeghem, J. Carrete, and N. Mingo, *Comput. Physics Commun.*, vol. 263, p. 107 945, 2021. DOI: 10.1016/j.cpc.2021.107945.

[vCO+2016] A. van Roekeghem, J. Carrete, C. Oses, S. Curtarolo, and N. Mingo, *Phys. Rev. X*, vol. 6, p. 041 061, 2016. DOI: 10.1103/PhysRevX.6.041061.

[WCMM2019] T. Wang, J. Carrete, N. Mingo, and G. K. H. Madsen, *ACS Appl. Mater. Interfaces.*, vol. 11, pp. 8175–8181, 2019. DOI: 10.1021/acsami.8b17525.

[WWK+2010] Y. Wang, L. L. Wang, S. Kong, M. Lazzeri, and F. Giustino, *J. Phys.: Condens. Matter*, vol. 22, p. 202 201, 2010. DOI: 10.1088/0953-8984/22/20/202201.

[WB2010] A. Ward and D. A. Broido, *Phys. Rev. B*, vol. 81, p. 085 205, 2010. DOI: 10.1103/PhysRevB.81.085205.

[WBSD2009] A. Ward, D. A. Broido, D. A. Stewart, and G. Deinzer, *Phys. Rev. B*, vol. 80, p. 125 203, 2009. DOI: 10.1103/PhysRevB.80.125203.

[XHB2014] H. Xie, M. Hu, and H. Bao, *Appl. Phys. Lett.*, vol. 104, 2014. DOI: 10.1063/1.4870586.

[ZA2014] D.-B. Zhang and P. B. Allen, *Phys. Rev. B*, vol. 90, p. 035 203, 2014. DOI: 10.1103/PhysRevB.90.035203.

[ZFM2007] W. Zhang, T. S. Fisher, and N. Mingo, *Numer. Heat Transf. B: Fundam.*, vol. 51, pp. 333–349, 2007. DOI: 10.1080/10407790601144755.

[ZNXO2014] F. Zhou, W. Nielson, Y. Xia, and V. Ozoliņš, *Phys. Rev. Lett.*, vol. 113, p. 185 501, 2014. DOI: 10.1103/PhysRevLett.113.185501.

[ZLL2016] L. Zhu, B. Li, and W. Li, *Physical Review B*, vol. 94, 2016, ISSN: 2469-9969. DOI: 10.1103/physrevb.94.115420. [Online]. Available: http://dx.doi.org/10.1103/PhysRevB.94.115420.

[Zim1960] J. Ziman, *Electrons and Phonons: The Theory of Transport Phenomena in Solids*. Oxford University Press, 1960, ISBN: 9780198512356.

[ZWFB1990] A. Zunger, S.-H. Wei, L. G. Ferreira, and J. E. Bernard, *Phys. Rev. Lett.*, vol. 65, pp. 353–356, 1990. DOI: 10.1103/PhysRevLett.65.353.